Received: 26 February 2021 | Revised: 7 July 2021 | Accepted: 14 July 2021

DOI: 10.1002/nme.6793

RESEARCH ARTICLE

WILEY

Hybrid equilibrium element with high-order stress fields for accurate elastic dynamic analysis

Francesco Parrinello | **Guido Borino**

Engineering Department, University of Palermo, Palermo, Italy

Correspondence
Francesco Parrinello, Engineering Department, University of Palermo, Viale delle Scienze, Ed. 8, Palermo 90128, Italy.
Email: francesco.parrinello@unipa.it

Abstract

In the present article the two-dimensional hybrid equilibrium element formulation is initially developed, with quadratic, cubic, and quartic stress fields, for static analysis of compressible and quasi-incompressible elastic solids in the variational framework of the minimum complementary energy principle. Thereafter, the high-order hybrid equilibrium formulation is developed for dynamic analysis of elastic solids in the variational framework of the Toupin principle, which is the complementary form of the Hamilton principle. The Newmark time integration scheme is introduced for discretization of the stress fields in the time domain and dynamic analysis of both the compressible solid and quasi-incompressible ones. The hybrid equilibrium element formulation provides very accurate solutions with a high-order stress field and the results of the static and dynamic analyses are compared with the solution of the classic displacement-based quadratic formulation, showing the convergence of the two formulations to the exact solution and the very satisfying performance of the proposed formulation, especially for analysis of quasi-incompressible elastic solids.

KEYWORDS

complementary form, dynamic analysis, equilibrium based, high-order stress, quasi-incompressible

1 | INTRODUCTION

The present article investigates the analysis of the elastodynamic problem using the stress-based approach of the hybrid equilibrium element formulation (HEE), which can be defined with high-order stress fields and can give great accuracy in stress computation. The equilibrium-based approach was introduced in the pioneering works of Fraeijs de Veubeke[1,2] for analysis of the elastic static problem and is defined in terms of stresses which implicitly satisfy domain and boundary equilibrium equations. The solution of the elastic static problem is determined in a weak form as a stationary condition of the complementary energy functional.

The equilibrium-based formulation was also developed in the hybrid form and several contributions[3-8] are available in the literature. In the hybrid equilibrium element (HEE) formulation, stress fields implicitly satisfy domain equilibrium equations and are independently defined for each finite element by polynomial stress functions of arbitrary order, with a set of so-called generalized stresses as degrees of freedom, which do not represent nodal values. The interelement equilibrium condition and the boundary equilibrium condition are imposed by the classic hybrid approach. The displacement

is defined at the element boundary, playing the role of a Lagrangian parameter. In order to accurately enforce interelement and boundary conditions, the displacement is assumed as a polynomial function of the same order as the stress and is independently defined for each element side, and therefore displacement can be discontinuous at the vertex between adjacent sides.

In HEE stress fields are defined as functions of the Cartesian coordinates, without any isoparametric mapping, even for elements with curved sides and the formulation is not pathologically influenced by the element distortion, but stress co-diffusivity at the curved sides cannot be strictly enforced. Moreover, the HEE formulation is particularly suitable for analysis of quasi-incompressible materials, for which the classic displacement based finite element formulation comes up against the well-known volumetric locking problems, especially for elements with linear interpolation (see Reference 9).

The great accuracy of the stress fields in HEE provides a powerful numerical tool for modeling of the interelement fracture propagation, as proposed by the author in Reference 10, where an extrinsic (initially rigid) cohesive interface is embedded at any element side without any remeshing and without additional degrees of freedom. In this case the analysis is limited to elastic static problems and its application to dynamic analysis of fracture and fragmentation phenomena would be of great interest. Indeed, analysis of such problems with classic intrinsic interface elements (see, e.g., References 11-13), with a penalty approach in the pre-failure regime, introduces additional compliance in elastic behavior with the relevant wave propagation issues. The dynamic fragmentation problem is approached by References 14,15 using the interelement fracture governed by means of a discontinuous Galerkin method, combined with an extrinsic interface.

The equilibrium-based solution of the linear elastic static problem with very high-order stress field is approached in Reference 16 by the mixed spectral element formulation, in which the symmetry of stress tensor is not assumed a priori, and displacement and rotation are defined as Lagrangian parameters enforcing the forces equilibrium condition in a strong form and the moments equilibrium condition, that is the stress symmetry condition, only weakly. The degrees of freedom for the stress are integrated traction components and stress is co-diffusive between elements. The mixed spectral element formulation is also proposed in hybrid form in Reference 17 with the target of reducing its computational cost without the introduction of spurious kinematic modes.

The typical drawback of the HEE is the possible occurrence of spurious kinematic modes, which must be controlled or restrained by means of one of the different available strategies.[18-21]

The finite element formulation of the elastic-dynamic problem in the framework of stress-based approaches, such as the hybrid equilibrium element method,[10,18] was addressed a few decades ago in References 22,23 and it currently remains a topic of great interest, as evidenced by recent articles.[24-29] In Reference 25 three alternative hybrid finite element formulations (hybrid-mixed, hybrid, and hybrid-Treftz) are presented and compared for solution of linear elastodynamic problems in the frequency domain, and these formulations are developed both in the displacement-based (DB) form and in the stress-based one. In Reference 26 the hybrid finite element formulation is applied for analysis of free and forced vibration problems, with independent approximation of the stresses, in the domain of the element, and of continuous displacements on the element boundary. The pointwise acceleration function is determined as the inertial term in the dynamic equilibrium equation and is defined as a function of the stress approximation. More recently, a hybrid stress triangular finite element was proposed in Reference 28 with independent displacement, rotation, and stress fields for elastic static analysis and for elastic dynamic analysis. The rotation field is introduced in order to enforce the symmetry of the stress tensor, which is modeled through the Raviart–Thomas vector basis functions[30] in its lowest order.

In Reference 27 a new complementary energy principle for elastodynamics is proposed with stresses and inertial forces considered as variables, for analysis of both free and forced vibration problems relating to compressible and incompressible elastic materials. The dynamic formulation of the HEE was introduced in Reference 31 for the solution of elastodynamic problems in the frequency domain, while the solution in the time domain is simply outlined. Moreover, the formulation is developed with linear, quadratic, cubic, and quartic stress approximations and with decomposition of stress in the static component, implicitly satisfying the static equilibrium equations, and in the dynamic one in equilibrium with the inertial forces. The same formulation is also presented and tested in Reference 32.

The novelty of the present article is the formulation of the hybrid dynamic equilibrium element in terms of a stress field without decomposition in the static and dynamic components and with the following high-order polynomial approximation: quadratic stress field (HEE2), cubic stress field (HEE3), and quartic stress field (HEE4). The proposed dynamic formulation of the HEE is rigorously developed in the variational framework of Toupin's principle,[33] which is a complementary form of Hamilton's principle. The proposed formulation with the three high-order stress fields is implemented in an open source finite element code for the solution of elastodynamic problem in the time domain. Several numerical simulations of compressible and quasi-incompressible materials are performed and the results are analyzed and critically compared with the solution of nine-node displacement based finite elements.

The article is organized as follows: in Section 2 the HEE is developed for analysis of the elastic static problem with quadratic, cubic, and quartic stress fields; in Section 3 the proposed formulation is developed for analysis of the elastic dynamic problem in the time domain; in Section 4 some numerical simulations are presented the analysis of static and dynamic problems of both compressible and quasi-incompressible materials; Section 5 reports the conclusions and includes a discussion of future developments; finally, the appendix reports some details of the numerical formulation.

2 | STATIC HYBRID EQUILIBRIUM FORMULATION

Let us consider a 2D elastic body occupying the closed region Ω. The body is referred to a Cartesian reference system (x, y) and is subjected to body force $\boldsymbol{b}(\boldsymbol{x}, \tau)$ in Ω , traction $\boldsymbol{t}(\boldsymbol{x}, \tau)$ on the free boundary Γ_T, imposed displacement $\overline{\mathbf{u}}(\tau)$ on the constrained boundary Γ_U and time $\tau \in (t_0, t)$. The equilibrium formulation belongs to the class of stress-based approaches and the weak form solution of the elastostatic problem is given as the stationary condition of the complementary energy functional, with stress fields satisfying the domain and boundary equilibrium equations.

The two-dimensional static equilibrium formulation considered in the present article follows the same reasoning path as proposed in References 10,18. The two-dimensional domain is discretized by a set of N_e nonoverlapping triangular subdomains Ω_e, with $\bigcup_{e=1}^{N_e} \Omega_e = \Omega$. The element subdomain boundary $\Gamma^e = \partial\Omega_e$ is composed of three sides Γ_s^e with $s = 1, 2, 3$, each of which can lie at the free boundary $\Gamma_s^e \subset \Gamma_T$, or can lie at the constrained boundary $\Gamma_s^e \subset \Gamma_U$, or can be an internal side between two subdomains $\Gamma_{int} \equiv \partial\Omega e_1 \cap \partial\Omega e_2$, with $e_1 \neq e_2$.

The hybrid approach of the equilibrium formulation is developed with the stress fields $\boldsymbol{\sigma}_e$ independently defined and satisfying the equilibrium equation in each subdomain (Div $\boldsymbol{\sigma}_e + \boldsymbol{b}_e = \mathbf{0}$ in Ω_e). The interelement equilibrium condition at all internal sides and the boundary equilibrium condition at all free boundary sides are imposed by the classical hybrid formulation, for which independent displacement fields $\boldsymbol{u}_s^e(\mathbf{x})$ are defined for each element side Γ_s^e, and they are assumed as Lagrangian variables in order to mutually connect adjacent elements or to apply traction on the free boundary (see, e.g., References 5,7,10,18,19). For the triangular finite element discretization, the hybrid equilibrium formulation gives the following modified complementary energy functional:

$$\overline{\Pi}_c = \sum_{e=1}^{N_e} \left[\frac{1}{2} \int_{\Omega_e} \boldsymbol{\sigma}^e : \mathbf{D} : \boldsymbol{\sigma}^e \, d\Omega - \sum_{s=1}^{3} \left(\int_{\Gamma_s^e} \boldsymbol{n}_s^e \cdot \boldsymbol{\sigma}^e \cdot \boldsymbol{u}_s^e \, d\Gamma - \int_{\Gamma_s^e \cap \Gamma_T} \boldsymbol{t} \cdot \boldsymbol{u}_s^e \, d\Gamma \right) \right] \tag{1}$$

with $\boldsymbol{u}_s^e = \overline{\boldsymbol{u}}$ on $\Gamma_s^e \cap \Gamma_U$ and $\boldsymbol{n}_s^e$ the outward unit vector normal to side Γ_s^e.

The stationary condition of the functional $\overline{\Pi}_c$, with respect to the Lagrangian variable $\boldsymbol{u}_s$ gives the weak form of the interelement equilibrium condition for an internal side and the weak form of the boundary equilibrium condition for a free boundary side. The stationary conditions of the functional $\overline{\Pi}_c$, with respect to the stress tensor $\boldsymbol{\sigma}^e$ provides a weak form of the compatibility condition between elastic strains $\boldsymbol{\varepsilon}^e = \mathbf{D} : \boldsymbol{\sigma}^e$ and displacement at the boundary sides $\boldsymbol{u}_{s=1,3}^e$. Details of the static formulation are given in References 10,18.

In hybrid equilibrium formulations the finite element is defined by the element stress fields satisfying the domain equilibrium equation, which does not interpolate nodal degrees of freedom, but is a function of generalized stresses. In the present article, the hybrid equilibrium element is developed only for two-dimensional membrane problems with polynomial stress fields of order $n_s = 2, 3, 4$.

Let a triangular finite element of domain Ω_e be considered and referred to a local Cartesian reference (x, y) centered at vertex 1, as shown in Figure 1A–C. The quadratic stress fields ($n_s = 2$) of a two-dimensional element are defined by the following polynomial functions

$$\sigma_x = a_1 + a_2 y + a_3 y^2 - a_9 x - a_{10} x^2/2 - 2a_{12} xy - b_x, \tag{2}$$

$$\sigma_y = a_4 + a_5 x + a_6 x^2 - a_8 y - a_{10} y^2/2 - 2a_{11} xy - b_y, \tag{3}$$

$$\tau_{xy} = a_7 + a_8 x + a_9 y + 2a_{10} xy + a_{11} x^2 + a_{12} y^2, \tag{4}$$

where b_x and b_y are components of uniform volume force on the element, and terms $a_1, \ldots, a_{12}$ are generalized stress variables. The stress fields of Equations (2)–(4) implicitly satisfy the domain equilibrium equation and for the eth element can be represented in the following Voigt notation

$$\boldsymbol{\sigma}_e(\mathbf{x}) = \mathbf{S}_e(\mathbf{x}) \cdot \mathbf{a}_e + \boldsymbol{\sigma}_e^0, \tag{5}$$

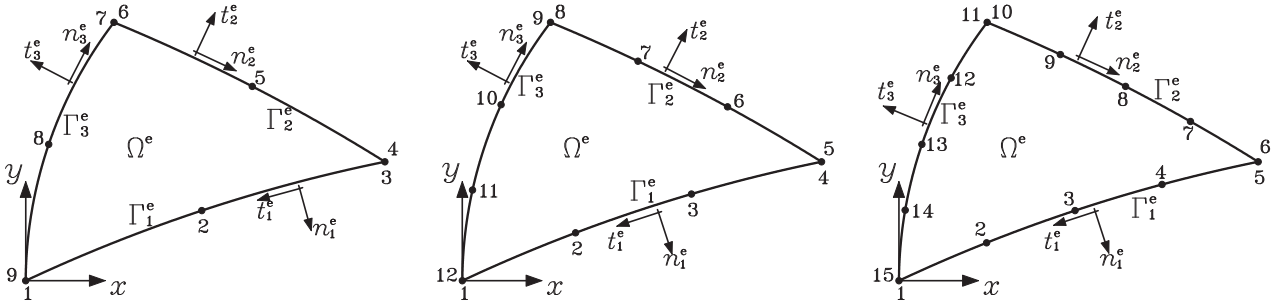

FIGURE 1 Nine-node, 12-node, and 15-node triangular hybrid equilibrium elements (HEE)

where $\mathbf{S}_e(\mathbf{x})$ is the coefficient matrix, $\mathbf{a}_e$ (of dimension $n_a = 12$) collects all generalized stress variables, and $\boldsymbol{\sigma}_e^0 = \left[-b_x, -b_y, 0\right]^T$ is a particular solution of the domain equilibrium equation, due to a uniform body force, and $\boldsymbol{\sigma}_e = \left[\sigma_x^e, \sigma_y^e, \tau_{xy}^e\right]^T$. The proposed formulation still satisfies the equilibrium equations if nonuniform body forces are considered, but only with polynomial function of order lower than that of stress formulation. The cubic and quartic stress fields are analogously defined and the dimension of generalized stress vector $\mathbf{a}_e$ is $n_a = 18$ for the cubic stress and $n_a = 24$ for the quartic one. See Appendix for the respective forms of the matrix $\mathbf{S}_e(\mathbf{x})$ and vector $\mathbf{a}_e$ in the quadratic, cubic, and quartic stress field formulations.

Displacement is independently defined at each element side and continuity at the vertexes is not imposed. In the proposed stress-based approach, equilibrium conditions are satisfied, whereas displacement continuity can only be weakly imposed. The geometry and displacement components of the element sides Γ_s^e with $s = 1, 2, 3$ are modeled by a classic isoparametric mapping

$$\boldsymbol{x}_s(\xi) = \sum_{n=1}^{n_u} N_n(\xi)\, \mathbf{X}_m^s = \mathbf{N}(\xi) \cdot \mathbf{x}_s^e, \tag{6}$$

$$\boldsymbol{u}_s(\xi) = \sum_{n=1}^{n_u} N_n(\xi)\, \mathbf{U}_m^s = \mathbf{N}(\xi) \cdot \mathbf{u}_s^e, \tag{7}$$

where n_u is the number of nodes per side; $m = n_u(s-1) + n$ is the node number; $N_n(\xi)$ is the nth shape function (polynomial function of order $n_d = n_u - 1$) in the parental coordinate $-1 \le \xi \le 1$; $\mathbf{U}_m^s$ and $\mathbf{X}_m^s$ respectively are the displacement and the Cartesian coordinate vectors of node m; $\mathbf{N}$ is the matrix collecting the shape functions and the vectors $\mathbf{x}_s^e$, $\mathbf{u}_s^e$ collect respectively coordinates and kinematic degrees of freedom of side Γ_s^e.

The complementary energy functional $\overline{\Pi}_c$ of Equation (1) can be written in the discretized form as

$$\overline{\Pi}_c = \sum_{e=1}^{n_e} \left[\frac{1}{2}\mathbf{a}_e^T \mathbf{C}_e \mathbf{a}_e - \mathbf{a}_e^T \mathbf{H}_e \mathbf{u}_e + \mathbf{T}_e^T \mathbf{u}_e\right], \tag{8}$$

where

$$\mathbf{C}_e = \int_{\Omega_e} \mathbf{S}_e^T \mathbf{D}\, \mathbf{S}_e d\Omega, \tag{9}$$

$$\mathbf{H}_e = \left[\mathbf{h}_1^e, \mathbf{h}_2^e, \mathbf{h}_3^e\right] \text{ with } \mathbf{h}_s^e = \int_{\Gamma_s^e} \mathbf{S}_e^T \mathbf{n}_s^e \mathbf{N} d\Gamma, \tag{10}$$

$$\mathbf{T}_e = \left[\mathbf{t}_1^e, \mathbf{t}_2^e, \mathbf{t}_3^e\right] \text{ with } \mathbf{t}_s^e = \int_{\Gamma_s^e \cap \Gamma_T} \mathbf{N}^T \boldsymbol{t} d\Gamma, \tag{11}$$

$$\mathbf{u}_e = \left[\mathbf{u}_1^e, \mathbf{u}_2^e, \mathbf{u}_3^e\right], \tag{12}$$

$$\mathbf{n}_s^e = \begin{bmatrix} n_{s1}^e & 0 \\ 0 & n_{s2}^e \\ n_{s2}^e & n_{s1}^e \end{bmatrix}. \tag{13}$$

The degrees of freedom of the fixed boundaries $\Gamma_s^e \subset \Gamma_U$ are constrained, with assigned value $\overline{\mathbf{u}}$. The stationary condition of function $\overline{\Pi}_c$ in Equation (8) with respect to the generalized stress vector $\mathbf{a}_e$ gives the following element equation of the discretized static hybrid equilibrium formulation

$$\frac{\partial \overline{\Pi}_c}{\partial \mathbf{a}_e} = \mathbf{C}_e \mathbf{a}_e - \mathbf{H}_e \mathbf{u}_e = \mathbf{C}_e \mathbf{a}_e - \mathbf{h}_1^e \mathbf{u}_1^e - \mathbf{h}_2^e \mathbf{u}_2^e - \mathbf{h}_3^e \mathbf{u}_3^e = \mathbf{0}, \tag{14}$$

which states the relationship between nodal displacement and generalized stress variables at the element level. The element nodal force vector can also be written as $\mathbf{q}_e = \mathbf{H}_e^T \mathbf{a}_e$ and the equation of the single hybrid equilibrium element is

$$\begin{bmatrix} \mathbf{C}_e & -\mathbf{H}_e \\ -\mathbf{H}_e^T & \mathbf{0} \end{bmatrix} \begin{bmatrix} \mathbf{a}_e \\ \mathbf{u}_e \end{bmatrix} = \begin{bmatrix} \mathbf{0} \\ -\mathbf{q}_e \end{bmatrix}, \tag{15}$$

where the compliance matrix $\mathbf{C}_e$ is symmetric, positive definite and not singular, so that it can be inverted and the generalized stress $\mathbf{a}_e$ can be condensed out at the element level, that is, mathematically

$$\mathbf{a}_e = \mathbf{C}_e^{-1} \mathbf{H}_e \mathbf{u}_e, \tag{16}$$

$$\mathbf{q}_e = \mathbf{H}_e^T \mathbf{C}_e^{-1} \mathbf{H}_e \mathbf{u}_e = \mathbf{K}_e \mathbf{u}_e, \tag{17}$$

where the matrix $\mathbf{K}_e = \mathbf{H}_e^T \mathbf{C}_e^{-1} \mathbf{H}_e$ is the element stiffness matrix and the HEE can be implemented in a classic displacement-based finite element code.

The use of the same order for the stress fields and for displacement of side ($n_s = n_d$) allows the proposed formulation accurately to verify the interelement equilibrium condition, with co-diffusive stresses $\boldsymbol{\sigma}^{e_1}$ and $\boldsymbol{\sigma}^{e_2}$ through the interelement side $\Gamma_{int} = \partial\Omega_{e_1} \cap \partial\Omega_{e_2}$. Therefore, in order to impose the interelement equilibrium condition, the nine-node HEE in Figure 1A is employed with a quadratic stress field, while the 12-node HEE in Figure 1B is employed a with cubic stress field, and the 15-node HEE in Figure 1C is employed with a quartic stress field.

The proposed HEE formulation is suitable for analysis of quasi-incompressible materials, whereas it fails to analyze the pure incompressible elastic problem. According to Reference 31 (sec. 4.7), for Poisson ratio $\nu = 0.5$ the compliance matrix C_e is rank deficient by one, due to the uniform hydrostatic stress field, which gives null complementary elastic strain energy. As a consequence, the element stiffness matrix K_e obtained by the static condensation in Equation (17) and depending on the inverse of compliance matrix, cannot be evaluated for incompressible elastic solids. In the same Reference 31 (sec. 4.7) an alternative strategy is proposed for the analysis of pure incompressible elastic problem, that is based on elimination of the uniform hydrostatic stress component in the stress basis and reduces the vector of generalized stress $\mathbf{a}_e$ by one (i.e., $n_a = 11$ for the quadratic stress field, $n_a = 17$ for the cubic one, and $n_a = 23$ for the quartic one). However, such approach can produces rank deficiency in the stiffness matrix and the solution uniqueness cannot be always guaranteed in terms of displacement. Therefore, the static and dynamic analyses of pure incompressible elastic problem are not tackled in the present article, but they represent an interesting topic for further development of the HEE formulation.

3 | THE DYNAMIC EQUILIBRIUM FORMULATION

The HEE static formulation has been developed and implemented with high-order polynomial stress fields and this fine accuracy would also be of great interest for dynamic analysis of elastic bodies. The finite element formulation of the elastic-dynamic problem, in the framework of stress-based approaches, has been proposed by several authors[22-29] and it can be rigorously developed in the variational framework of Toupin's principle,[33] which is a complementary form of Hamilton's principle.[34] In Toupin's principle the velocity, and therefore the kinetic energy density, are defined as functions the time integral of stress, which is the areal density of the impulse $\boldsymbol{J}(t) = \int_{t_0}^{t} \boldsymbol{\sigma} d\tau$ or, instead, the stresses are defined as time derivatives of the impulse as $\boldsymbol{\sigma} = \dot{\boldsymbol{J}}$. Therefore the dynamic equilibrium equation can be written as follows:

$$\text{div}\, \boldsymbol{\sigma} + \boldsymbol{b} - \rho \ddot{\boldsymbol{u}} = \text{div}\, \dot{\boldsymbol{J}} + \boldsymbol{b} - \rho \ddot{\boldsymbol{u}} = \mathbf{0}, \tag{18}$$

where ρ is the mass density. After time integration and with null velocity at initial conditions ($\dot{\boldsymbol{u}}(t_0) = \dot{\boldsymbol{u}}_0 = \boldsymbol{0}$) the following relationship between impulse and velocity can be stated:

$$\dot{\boldsymbol{u}} = \frac{1}{\rho}\left(\operatorname{div}\boldsymbol{J} + \overline{\boldsymbol{b}}\right) \tag{19}$$

with $\overline{\boldsymbol{b}} = \int_{t_0}^{t} \boldsymbol{b} d\tau$; the kinetic energy at time t can be defined as

$$T(\boldsymbol{J}, t) = \int_{\Omega} \frac{1}{2}\rho\dot{\boldsymbol{u}}\cdot\dot{\boldsymbol{u}} d\Omega = \int_{\Omega} \frac{1}{2\rho}\left(\operatorname{div}\boldsymbol{J} + \overline{\boldsymbol{b}}\right)\cdot\left(\operatorname{div}\boldsymbol{J} + \overline{\boldsymbol{b}}\right) d\Omega, \tag{20}$$

whereas the complementary potential energy is defined as a function of the time derivative of the impulse tensor in the following form:

$$\Pi_c\left(\dot{\boldsymbol{J}}, t\right) = \int_{\Omega} \frac{1}{2}\dot{\boldsymbol{J}} : \mathbf{D} : \dot{\boldsymbol{J}} d\Omega - \int_{\Gamma_U} \boldsymbol{n}\cdot\dot{\boldsymbol{J}}\cdot\overline{\boldsymbol{u}} d\Gamma, \tag{21}$$

where the impulse implicitly verifies the free boundary equilibrium equation ($\dot{\boldsymbol{J}}\cdot\boldsymbol{n} = \boldsymbol{t}$ on $\Gamma_T \times (t_0, t)$), $\boldsymbol{n}$ is the outward unit vector normal to the external surface $\Gamma = \Gamma_T \cup \Gamma_U$ and $\overline{\boldsymbol{u}}(t)$ is the imposed displacement at the constrained surface Γ_U.

Finally, the complementary form of the Hamilton functional is defined as

$$H_c\left(\boldsymbol{J}, \dot{\boldsymbol{J}}\right) = \int_{t_0}^{t} T(\boldsymbol{J}, \tau) - \Pi_c\left(\dot{\boldsymbol{J}}, \tau\right) d\tau \tag{22}$$

and the variational approach of the dynamic response of the elastic solid is given in terms of the impulse tensor $\boldsymbol{J}(\boldsymbol{x}, \tau)$ defined in the domain $\Omega \times (t_0, t)$, which implicitly verifies the free boundary equilibrium condition and for which the first variation of the functional in Equation (22) is null, that is

$$\begin{aligned}
\delta H_c\left(\boldsymbol{J}, \dot{\boldsymbol{J}}\right) &= \int_{t_0}^{t} \delta T(\boldsymbol{J}, \tau) - \delta\Pi_c\left(\dot{\boldsymbol{J}}, \tau\right) d\tau = \\
&= \iint_{\Omega\times(t_0,t)} \frac{1}{\rho}\left(\operatorname{div}\boldsymbol{J} + \overline{\boldsymbol{b}}\right)\cdot\operatorname{div}\delta\boldsymbol{J} d\Omega d\tau - \iint_{\Omega\times(t_0,t)} \dot{\boldsymbol{J}} : \mathbf{D} : \delta\dot{\boldsymbol{J}} d\Omega d\tau \\
&\quad + \iint_{\Gamma_U\times(t_0,t)} \boldsymbol{n}\cdot\delta\dot{\boldsymbol{J}}\cdot\overline{\boldsymbol{u}} d\Gamma d\tau = 0 \quad \forall \quad \delta\boldsymbol{J} \neq \boldsymbol{0} \\
s.t.\ \ & \delta\dot{\boldsymbol{J}}(\boldsymbol{x}, \tau)\cdot\boldsymbol{n} = \boldsymbol{0} \text{ in } \Gamma_T \times (t_0, t), \\
& \delta\boldsymbol{J}(\boldsymbol{x}, t_0) = \delta\boldsymbol{J}(\boldsymbol{x}, t) = \boldsymbol{0} \ \text{ in } \ \Omega.
\end{aligned} \tag{23}$$

The stationary condition in Equation (23) of the variational approach, after integration by part with respect to the time variable and using the divergence theorem, can be rewritten in the following form:

$$\begin{aligned}
\delta H_c\left(\boldsymbol{J}, \ddot{\boldsymbol{J}}\right) = & \iint_{\Gamma_U\times(t_0,t)} \left[\frac{1}{\rho}\left(\operatorname{div}\boldsymbol{J} + \overline{\boldsymbol{b}}\right) - \dot{\overline{\boldsymbol{u}}}\right]\cdot\delta\boldsymbol{J}\cdot\boldsymbol{n} d\Gamma d\tau \\
& - \iint_{\Omega\times(t_0,t)} \left[\nabla_s \frac{1}{\rho}\left(\operatorname{div}\boldsymbol{J} + \overline{\boldsymbol{b}}\right) - \mathbf{D} : \ddot{\boldsymbol{J}}\right] : \delta\boldsymbol{J} d\Gamma d\tau = \boldsymbol{0} \quad \forall \quad \delta\boldsymbol{J} \neq \boldsymbol{0},
\end{aligned} \tag{24}$$

where the symmetric gradient operator (∇_s) emerges from the symmetry of tensor $\delta\boldsymbol{J}$ and the conditions $\delta\boldsymbol{J}(\boldsymbol{x}, t_0) = \delta\boldsymbol{J}(\boldsymbol{x}, t) = \boldsymbol{0}$ in Ω and $\delta\boldsymbol{J}(\boldsymbol{x}, \tau)\cdot\boldsymbol{n} = \boldsymbol{0}$ in $\Gamma_T \times (t_0, t)$ have been considered. Due to Equation (19), the first integral of Equation (24) provides the weak form of the kinematic boundary condition, that is

$$\iint_{\Gamma_U\times(t_0,t)} \left(\dot{\boldsymbol{u}} - \dot{\overline{\boldsymbol{u}}}\right)\cdot\delta\boldsymbol{J}\cdot\boldsymbol{n}\, d\Gamma\, d\tau = \boldsymbol{0} \quad \forall \quad \delta\boldsymbol{J} \neq \boldsymbol{0} \tag{25}$$

and the second integral of Equation (24) provides the weak form of the strain–displacement kinematic conditions, that is

$$\iint_{\Omega\times(t_0,t)} [\nabla_s \dot{\boldsymbol{u}} - \dot{\boldsymbol{\varepsilon}}] : \delta \boldsymbol{J}\, d\Gamma\, d\tau = \boldsymbol{0} \quad \forall \quad \delta \boldsymbol{J} \neq \boldsymbol{0} \tag{26}$$

with the strain rate given by the elastic constitutive equation $\dot{\boldsymbol{\varepsilon}} = \mathbf{D} : \dot{\boldsymbol{\sigma}} = \mathbf{D} : \ddot{\boldsymbol{J}}$. Equations (18) and (24) with the elastic constitutive equation and under the hypothesis of the free boundary equilibrium condition implicitly satisfied, constitute the weak form of the partial differential governing equations of the dynamic formulation of the solid elastic problem.

3.1 | The dynamic hybrid equilibrium element

The complementary form of the two-dimensional dynamic problem is developed in the present article by a hybrid finite element formulation similar to the static one. The domain discretization is considered with a set of N_e nonoverlapping triangular subdomains Ω_e, with $\bigcup_{e=1}^{N_e} \Omega_e = \Omega$. The impulse field (with the relevant stress field) is independently defined in each subdomain as $\boldsymbol{J}_e(\boldsymbol{x})$ in Ω_e and it does not implicitly verify the free boundary equilibrium equation. The interelement equilibrium condition at all internal sides and the boundary equilibrium condition at all free boundary sides are imposed in the same way as in the quasi-static formulation.[4,18,35] Therefore, an independent displacement field $\boldsymbol{u}_s^e(\mathbf{x})$ is defined for each element side Γ_s^e, and it is assumed as a Lagrangian variable in order to mutually connect adjacent elements or to apply traction on the free boundary.

The hybrid dynamic equilibrium formulation with the assumed domain discretization gives the following hybrid form of the complementary Hamilton functional (or Toupin functional) (see References 22,23,31,33,36)

$$\begin{aligned}\overline{H}_c\left(\boldsymbol{J}_e, \boldsymbol{u}_s^e\right) = \int_{t_0}^{t} \sum_{e=1}^{N_e} \Bigg[& \int_{\Omega_e} \frac{1}{2\rho} \left(\operatorname{div} \boldsymbol{J}_e + \overline{\boldsymbol{b}}_e\right) \cdot \left(\operatorname{div} \boldsymbol{J}_e + \overline{\boldsymbol{b}}_e\right) d\Omega \\ & - \int_{\Omega_e} \frac{1}{2} \dot{\boldsymbol{J}}_e : \mathbf{D} : \dot{\boldsymbol{J}}_e d\Omega + \sum_{s=1}^{3} \left(\int_{\Gamma_s^e} \boldsymbol{n}_s^e \cdot \dot{\boldsymbol{J}}_e \cdot \boldsymbol{u}_s^e \, d\Gamma - \int_{\Gamma_s^e \cap \Gamma_T} \boldsymbol{t} \cdot \boldsymbol{u}_s^e \, d\Gamma \right) \Bigg] d\tau \end{aligned} \tag{27}$$

with $\boldsymbol{u}_s^e = \overline{\boldsymbol{u}}$ on $\Gamma_s^e \cap \Gamma_U$ and $\boldsymbol{n}_s^e$ the outward normal to side Γ_s^e.

The stationary condition of this functional with respect to a single domain impulse field $\boldsymbol{J}_e$ gives the same weak form in Equation (24), but limited to the subdomain Ω_e, whereas the stationary condition with respect to the displacement field $\boldsymbol{u}_s$ at the internal side between two adjacent subdomains $\Gamma_s = \Omega_{e_1} \cap \Omega_{e_1}$ produces the following weak form of the interelement equilibrium condition:

$$\iint_{\Gamma_s\times(t_0,t)} \boldsymbol{n}_s \cdot \left(\dot{\boldsymbol{J}}_{e_1} - \dot{\boldsymbol{J}}_{e_2}\right) \cdot \delta \boldsymbol{u}_s \, d\Gamma d\tau = 0 \quad \forall \quad \delta \boldsymbol{u}_s, \tag{28}$$

where $\boldsymbol{n}_s = \boldsymbol{n}_s^{e_1} = -\boldsymbol{n}_s^{e_2}$. Finally, the stationary condition of the functional in Equation (27) with respect to the displacement field of a free boundary sides $\Gamma_s^e \cup \Gamma_T$ produces the following weak form of the free boundary equilibrium equation

$$\iint_{\Gamma_s^e\times(t_0,t)} \left(\boldsymbol{n}_s^e \cdot \dot{\boldsymbol{J}}_e - \boldsymbol{t}\right) \cdot \delta \boldsymbol{u}_s^e \, d\Gamma d\tau = 0 \quad \forall \quad \delta \boldsymbol{u}_s^e. \tag{29}$$

The hybrid dynamic equilibrium finite element formulation, based on Toupin's principle, is proposed in Reference 31 with the decomposition of the impulse field into the static and dynamic parts $\boldsymbol{J}_e = \boldsymbol{J}_e^d + \boldsymbol{J}_e^s$, where the static field implicitly verifies the domain equilibrium equation ($\operatorname{div} \boldsymbol{J}_e^s + \overline{\boldsymbol{b}}_e = \boldsymbol{0}$ in Ω_e). The stress decomposition is also proposed in Reference 32 for analysis of the elastic-dynamic problem in the frequency domain and the estimation of the eigenfrequencies is improved by the combination of two dual formulations, that are the compatible DB finite element model and the equilibrated one. In References 31,32 the elastic-dynamic problem is analyzed in the frequency domain, where decomposition of the impulse field allows to remove the zero eigenvalues. In fact, the static component ($\boldsymbol{J}_e^s$) produces a null partition in

the mobility matrix (defined in Equation (35)) with the relevant zero eigenvalues, whereas the dynamic component ($\boldsymbol{J}_e^d$) provides a full-rank mobility matrix.

In the present article the elastic-dynamic problem is analyzed in the time domain where the decomposition of the impulse field is an additional and not necessary computational effort. Therefore for each subdomain Ω_e a quadratic polynomial law is assumed for all the components of the impulse tensor, which can be written in the following Voigt's notation:

$$\mathbf{J}_e(\boldsymbol{x},\tau)=\begin{bmatrix}J_x\\J_y\\J_{xy}\end{bmatrix}=\begin{bmatrix}a_1+a_4x+a_7y+a_{10}xy+a_{13}x^2+a_{16}y^2\\a_2+a_5x+a_8y+a_{11}xy+a_{14}x^2+a_{17}y^2\\a_3+a_6x+a_9y+a_{12}xy+a_{15}x^2+a_{18}y^2\end{bmatrix}=\mathbf{S}_e(\boldsymbol{x})\,\mathbf{a}_e(\tau), \tag{30}$$

where $\mathbf{a}_e(\tau)=[a_1(\tau),\ \dots\ ,a_{18}(\tau)]$ collects the generalized impulse time-dependent functions $a_i(\tau)$ and $\mathbf{S}_e$ collects the polynomial terms. Moreover, the stress field is defined as the time derivative of the impulse, and is simply defied as

$$\boldsymbol{\sigma}_e(\boldsymbol{x},\tau)=\dot{\mathbf{J}}_e(\boldsymbol{x},\tau)=\mathbf{S}_e(\boldsymbol{x})\,\dot{\mathbf{a}}_e(\tau) \tag{31}$$

and the divergence of the impulse law, in Voigt notation, is defined as

$$\operatorname{div}\boldsymbol{J}_e(\boldsymbol{x},\tau)=\begin{bmatrix}J_{x,x}+J_{xy,y}\\J_{xy,x}+J_{y,y}\end{bmatrix}=\mathbf{T}_e(\boldsymbol{x})\,\mathbf{a}_e(\tau) \tag{32}$$

with

$$\mathbf{T}_e=\begin{bmatrix}0&0&0&1&0&0&0&0&1&y&0&x&2x&0&0&0&0&2y\\0&0&0&0&0&1&0&1&0&0&x&y&0&0&2x&0&2y&0\end{bmatrix}. \tag{33}$$

See Appendix for the respective forms of the matrices $\mathbf{S}_e(\mathbf{x})$ and $\mathbf{T}_e(\mathbf{x})$ in the quadratic, cubic, and quartic stress field formulations. In hybrid dynamic equilibrium formulations the finite element is defined by the element impulse and stress fields which do not interpolate nodal degrees of freedom, but are functions of generalized time-dependent variables $a_i(\tau)$. In the present article, the proposed formulation is developed for two-dimensional membrane problems with polynomial impulse and stress fields of order $n_s=2,3,4$. The cubic and quartic stress fields are analogously defined and the dimension of generalized impulse vector $\mathbf{a}_e$ is $n_a=30$ for the cubic stress and $n_a=45$ for the quartic one.

The independent displacement fields at the element sides are defined by the same isoparametric formulation as adopted for the static solution in Equations (6) and (7), and the stationary condition of the complementary Hamilton functional in Equation (27), with respect to the vector of impulse field $\mathbf{a}_e(\tau)$, and with integration by part with respect to the time variable τ, is written in the following discretized form:

$$\int_{t_0}^{t}\delta\mathbf{a}_e^T\left[\mathbf{M}_e\mathbf{a}_e+\mathbf{f}_e+\mathbf{C}_e\ddot{\mathbf{a}}_e-\mathbf{H}_e\dot{\mathbf{u}}_e\right]d\tau=0\quad\forall\ \ \delta\mathbf{a}_e(\tau)\neq\mathbf{0}/\delta\mathbf{a}_e(t_0)=\delta\mathbf{a}_e(t)=\mathbf{0}, \tag{34}$$

where

$$\mathbf{M}_e=\int_{\Omega_e}\frac{1}{\rho}\mathbf{T}_e^T\mathbf{T}_e d\Omega \tag{35}$$

is termed mobility matrix in References 22,31 and can be interpreted as an inverse mass matrix;

$$\mathbf{C}_e=\int_{\Omega_e}\mathbf{S}_e^T\mathbf{D}\,\mathbf{S}_e d\Omega \tag{36}$$

is the compliance element matrix, which can be interpreted as an inverse stiffness matrix; the matrix $\mathbf{H}_e$ is the stress–displacement coupling matrix, which is defined in Equation (10) but with the matrix of polynomial function $\mathbf{S}_e(\boldsymbol{x})$

defined in Equation (30); finally

$$\mathbf{f}_e = \int_{\Omega_e} \frac{1}{\rho} \mathbf{T}_e^T \overline{\boldsymbol{b}}_e d\Omega \tag{37}$$

is the vector of the element domain integral of the time-integrated body force $\overline{\boldsymbol{b}}_e$.

The stationary condition of the complementary Hamilton functional in Equation (27), with respect to the vector of element side displacement $\mathbf{u}_e(\tau)$, is written in the following discretized form

$$\int_{t_0}^{t} \delta \mathbf{u}_e^T \left[\mathbf{q}_e - \mathbf{H}_e^T \dot{\mathbf{a}}_e \right] d\tau = 0 \quad \forall \quad \delta \mathbf{u}_e(\tau) \neq \mathbf{0} / \delta \mathbf{u}_e(t_0) = \delta \mathbf{u}_e(t) = \mathbf{0}, \tag{38}$$

where $\mathbf{q}_e$ is the vector of element nodal forces.

The dynamic hybrid equilibrium formulation, as well as the static one, maps impulse and stress fields as function of the Cartesian coordinate (x, y) and neither the spatial derivative nor the jacobian transformation are required in the formulation. As a consequence, the HEEs, in both static and dynamic formulations, are not pathologically sensitive to the element distortion.

3.2 | Integration in the time domain

The time domain (t_0, t) is discretized in a set of time intervals $\Delta t = t_{n+1} - t_n$ and for the first interval $(n = 0)$ the initial conditions are known in terms of a generalized impulse vector and its derivatives $\mathbf{a}_e^n$, $\dot{\mathbf{a}}_e^n$, and $\ddot{\mathbf{a}}_e^n$, and in terms of nodal displacement and velocity $\mathbf{u}_e^n$ and $\dot{\mathbf{u}}_e^n$. The objective of dynamic analysis is to obtain, for a generic time interval, the approximation of the generalized impulse vector and nodal displacement with the relevant derivatives at the end of time step ($\mathbf{a}_e^{n+1}$, $\dot{\mathbf{a}}_e^{n+1}$, $\ddot{\mathbf{a}}_e^{n+1}$, $\mathbf{u}_e^{n+1}$, and $\dot{\mathbf{u}}_e^{n+1}$) given the initial conditions at time t_n. For a generic time interval the two integrand functions are assumed to be identically null at the initial step condition, that is

$$\mathbf{M}_e \mathbf{a}_e^n + \mathbf{C}_e \ddot{\mathbf{a}}_e^n - \mathbf{H}_e \dot{\mathbf{u}}_e^n = -\mathbf{f}_e{}^n \tag{39}$$

$$\mathbf{H}_e^T \dot{\mathbf{a}}_e^n = \mathbf{q}_e^n. \tag{40}$$

The classic Newmark time integration procedure is considered for the generalized impulse vector

$$\mathbf{a}_e^{n+1} = \mathbf{a}_e^n + \dot{\mathbf{a}}_e^n \Delta t + \left(\frac{1}{2} - \beta \right) \ddot{\mathbf{a}}_e^n \Delta t^2 + \beta \ddot{\mathbf{a}}_e^{n+1} \Delta t^2 = \overline{\mathbf{a}}_e^{n+1} + \beta \ddot{\mathbf{a}}_e^{n+1} \Delta t^2, \tag{41}$$

$$\dot{\mathbf{a}}_e^{n+1} = \dot{\mathbf{a}}_e^n + (1 - \gamma) \ddot{\mathbf{a}}_e^n \Delta t + \gamma \ddot{\mathbf{a}}_e^{n+1} \Delta t, \tag{42}$$

where β and γ are the Newmark parameters and $\overline{\mathbf{a}}_e^{n+1} = \mathbf{a}_e^n + \dot{\mathbf{a}}_e^n \Delta t + \left(\frac{1}{2} - \beta \right) \ddot{\mathbf{a}}_e^n \Delta t^2$. The values of the two parameters are based on the constant-average-acceleration method originally assumed as unconditionally stable by Newmark, that are $\beta = 0.25$ and $\gamma = 0.5$. The nodal velocity is simply defined as

$$\dot{\mathbf{u}}_e^{n+1} = \frac{\mathbf{u}_e^{n+1} - \mathbf{u}_e^n}{\Delta t} = \frac{\Delta \mathbf{u}_e}{\Delta t} \tag{43}$$

and the integral Equations (34) and (38) can be solved in the form of the minimum weighted residual, which gives the following equation at the end of the time interval:

$$\mathbf{M}_e \mathbf{a}_e^{n+1} + \mathbf{C}_e \ddot{\mathbf{a}}_e^{n+1} - \mathbf{H}_e \dot{\mathbf{u}}_e^{n+1} = -\mathbf{f}_e{}^{n+1}, \tag{44}$$

$$\mathbf{H}_e^T \dot{\mathbf{a}}_e^{n+1} = \mathbf{q}_e^{n+1}. \tag{45}$$

where the vector $\mathbf{f}_e{}^{n+1}$ is defined in Equation (37) and the trapezoidal integration rule has been applied for the time integration of the body force

$$\overline{\boldsymbol{b}}_e{}^{n+1} = \overline{\boldsymbol{b}}_e{}^n + \int_{t_n}^{t_{n+1}} \boldsymbol{b}_e(\tau)\, d\tau = \overline{\boldsymbol{b}}_e{}^n + \frac{\boldsymbol{b}_e(t_n) + \boldsymbol{b}_e(t_{n+1})}{2} \Delta t. \tag{46}$$

After substitution of the Newmark time integration rules defined in Equations (41)–(43), the impulse vector and its first derivative can be written as function of the second time derivative of the impulse vector $\ddot{\mathbf{a}}_e^{n+1}$, so the Equations (44) and (45) can be written as

$$\left(\mathbf{M}_e\beta\Delta t^2+\mathbf{C}_e\right)\ddot{\mathbf{a}}_e^{n+1}+\mathbf{M}_e\bar{\ddot{\mathbf{a}}}_e^{n+1}-\mathbf{H}_e\frac{\Delta\mathbf{u}_e}{\Delta t}=-\mathbf{f}_e{}^{n+1}, \tag{47}$$

$$\mathbf{H}_e^T\ddot{\mathbf{a}}_e^{n+1}\gamma\Delta t=\mathbf{q}_e^{n+1}-\mathbf{H}_e^T\dot{\mathbf{a}}_e^n-\mathbf{H}_e^T\ddot{\mathbf{a}}_e^n\left(1-\gamma\right)\Delta t=\Delta\mathbf{q}_e-\mathbf{H}_e^T\ddot{\mathbf{a}}_e^n\left(1-\gamma\right)\Delta t, \tag{48}$$

where Equation (40) is considered. The last two equations can be rewritten in the following element matrix notation

$$\begin{bmatrix}\mathbf{M}_e\beta\Delta t^2+\mathbf{C}_e & -\mathbf{H}_e\\ -\mathbf{H}_e^T & \mathbf{0}\end{bmatrix}\begin{bmatrix}\ddot{\mathbf{a}}_e^{n+1}\\ \Delta\mathbf{u}_e/\Delta t\end{bmatrix}=\begin{bmatrix}-\mathbf{f}_e{}^{n+1}-\mathbf{M}_e\bar{\ddot{\mathbf{a}}}_e^{n+1}\\ -\Delta\mathbf{q}_e/\gamma\Delta t+\mathbf{H}_e^T\ddot{\mathbf{a}}_e^n\left(1-\gamma\right)/\gamma\end{bmatrix}, \tag{49}$$

where $\Delta\mathbf{q}_e=\mathbf{q}_e^{n+1}-\mathbf{q}_e^n$ is the increment of the nodal force vector and the solution unknowns are the second time derivative of the impulse vector $\ddot{\mathbf{a}}_e^{n+1}$ and the increment of element nodal displacement $\Delta\mathbf{u}_e$. Equation (49) represents the incremental finite element equation of the dynamic HEE, which can be solved by a monolithic solver or, in a simpler and less computationally expensive form, by the static condensation of the generalized impulse vector $\ddot{\mathbf{a}}_e^{n+1}$ out of the element equation, that is

$$\ddot{\mathbf{a}}_e^{n+1}=\left(\mathbf{M}_e\beta\Delta t^2+\mathbf{C}_e\right)^{-1}\left[\mathbf{H}_e\frac{\Delta\mathbf{u}_e}{\Delta t}-\mathbf{f}_e{}^{n+1}-\mathbf{M}_e\bar{\ddot{\mathbf{a}}}_e^{n+1}\right], \tag{50}$$

$$\begin{aligned}\Delta\mathbf{q}_e&=\gamma\mathbf{H}_e^T\left(\mathbf{M}_e\beta\Delta t^2+\mathbf{C}_e\right)^{-1}\mathbf{H}_e\Delta\mathbf{u}_e-\mathbf{H}_e^T\left(\mathbf{M}_e\beta\Delta t^2+\mathbf{C}_e\right)^{-1}\left[\mathbf{f}_e{}^{n+1}+\mathbf{M}_e\bar{\ddot{\mathbf{a}}}_e^{n+1}\right]\gamma\Delta t+\mathbf{H}_e^T\ddot{\mathbf{a}}_e^n\left(1-\gamma\right)\Delta t\\&=\mathbf{K}_e\Delta\mathbf{u}_e+\mathbf{r}_e,\end{aligned} \tag{51}$$

where

$$\mathbf{K}_e=\gamma\mathbf{H}_e^T\left(\mathbf{M}_e\beta\Delta t^2+\mathbf{C}_e\right)^{-1}\mathbf{H}_e \tag{52}$$

is the element dynamic stiffness matrix and

$$\mathbf{r}_e=-\mathbf{H}_e^T\left(\mathbf{M}_e\beta\Delta t^2+\mathbf{C}_e\right)^{-1}\left[\mathbf{f}_e{}^{n+1}+\mathbf{M}_e\bar{\ddot{\mathbf{a}}}_e^{n+1}\right]\gamma\Delta t+\mathbf{H}_e^T\ddot{\mathbf{a}}_e^n\left(1-\gamma\right)\Delta t \tag{53}$$

is the residual vector. Dynamic stiffness matrix and residual vector can be numerically evaluated with a simple static condensation procedure and can be implemented in a standard finite element code for the time-stepping analysis of the dynamic problem of elastic solids. The mobility matrix $\mathbf{M}_e$ is rank deficient and, as pointed out for the static analysis, the proposed formulation is suitable for analysis of quasi-incompressible materials, whereas it fails to analyze the pure incompressible elastic problem. In fact, for Poisson ratio $\nu=0.5$ the compliance matrix $\mathbf{C}_e$ and the sum of matrices $(\mathbf{M}_e\beta\Delta t^2+\mathbf{C}_e)$ are rank deficient, so the dynamic stiffness matrix $\mathbf{K}_e$ obtained by the static condensation in Equation (52) cannot be evaluated for incompressible elastic solids.

The proposed dynamic formulation is also applied for the modeling of time discontinuous load, whose solution in the equilibrium based formulation is governed by time discontinuous stress field. However, in the Newmark discretization of the time domain, the load discontinuity can be applied in a discretized form inside a single (small but finite) time increment $\Delta t>0$. The results of a numerical simulation with time discontinuous load, and with two different values of the time increment, are reported in the article.

Finally, the proposed formulation is based on the assumption of null initial condition, with null displacements and null velocities at time $t=t_0$ (loading step $n=0$), that are $\mathbf{u}_e\left(t_0\right)=\mathbf{u}_e^0=\mathbf{0}$ and $\dot{\mathbf{u}}_e\left(t_0\right)=\dot{\mathbf{u}}_e^0=\mathbf{0}$. In the case of a preloaded solid with initial elastic deformation associated to the nonzero initial conditions, the problem of the elastic static solid has to be preliminary solved and the relevant vectors of generalized stress $\dot{\mathbf{a}}_e\left(t_0\right)=\dot{\mathbf{a}}_e^{(0)}$ and $\bar{\ddot{\mathbf{a}}}_e^0=\dot{\mathbf{a}}_e^0\Delta t$ have to be evaluated for each finite element, for resolution of Equation (49). However, this problem is not addressed in the present article.

4 | NUMERICAL SIMULATION

The static and the dynamic formulations were implemented in the finite element code FEAP v8.5[37] using a triangular HEE with the quadratic, cubic, and quartic stress fields. In detail, the nine-node hybrid equilibrium element (HEE2) in Figure 1A is implemented with the quadratic stress field, while the 12-node element (HEE3) in Figure 1B is developed with the cubic stress field, and the 15-node element (HEE4) in Figure 1C with quartic stress field.

The performance of the proposed formulation with high-order stress field is illustrated by some static and dynamic analyses and the results are compared with the solutions obtained with the well-known nine-node quadrilateral displacement-based element.

To the authors' best knowledge, the HEE formulation with triangular two-dimensional elements can be affected by SKMs on well-known patches of elements, as described in References 18-21,35. These SKMs can be restrained by the approach proposed in Reference 18. The numerical simulations proposed in this article are based on meshes which can be affected only by the SKM on elements with two free boundary sides, that are the corners discretized by a single element. The SKM involves the two free boundary sides and can be restrained by a rigid constrain between the degrees of freedom of the two coincident nodes at the corners.

4.1 | Cook's membrane elastic-static problem

Cook's membrane, represented in Figure 2, is a classic two-dimensional elastic problem, initially proposed in Reference 38, and analyzed by several authors for the performance evaluation of the finite element formulations, as proposed in References 18,28,39,40. The structure is constrained at the left side and loaded at the right side by a unitary force which can be applied by several different traction boundary conditions, although it is generally applied as a uniformly distributed tangential load.[18,28,39] While the trend of the tangential traction field at the free boundary side is not of great importance in a displacement-based formulation, it is pivotal in the equilibrium-based approach.

At the two corners C_1 and C_2 represented in Figure 2, continuous and statically admissible stress fields (strictly enforcing the equilibrium equations) cannot be defined with the following boundary conditions: nonzero tangential stress $\tau_n \neq 0$, null tangential stress τ_m at the upper and lower sides, and null normal stresses $\sigma_m = \sigma_n = 0$. In fact, the two-dimensional stress tensor is defined by three independent components and only the null value $\tau_n = 0$ satisfy the equilibrium equations for a continuous stress field. The load with tangential stress $\tau_n \neq 0$ can be applied in a strict equilibrium condition if the two corners are discretized with two or more elements, with discontinuous stress fields.

The problem of tangential traction distribution at the right boundary side can be addressed by three different solutions:

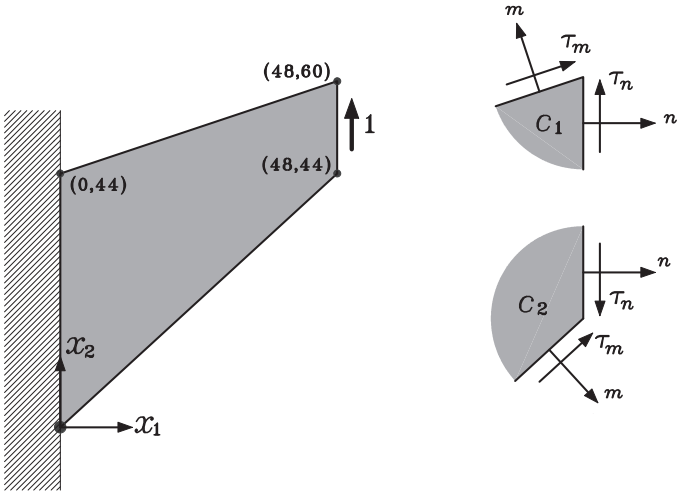

FIGURE 2 Sizes and geometry of the Cook membrane elastic problem

- a uniform tangential load, for which the exact solution is not regular at the corner, can be applied with discontinuous stress fields at the two corners, by splitting the corners in two or more finite elements;
- a quadratic tangential load with null values at the two corners, like the Jourawsky beam solution;
- the real distribution of tangential load can be neglected by considering the right side to be rigid in its own plane. This approach also overcomes the problem of the SKM at the single element corner, being a kinematic constrain such as that proposed in Reference 18.

Although the Cook's membrane problem is usually solved with the uniform tangential load, the third approach is preferred and computationally applied by a rigid link between all the vertical degrees of freedom of the right side; the unit tangential force is applied to a node of the vertically rigid side.

The two-dimensional numerical analyses were performed under plane strain conditions with the elastic parameters: $E = 1$, $\nu = 1/3$ for a volumetric compressible test and $E = 1$, $\nu = 0.4999$ for a quasi-incompressible test. Several discretizations were tested for both the HEE formulation and for displacement-based one and the details of the analyzed meshes, with the number of nodes, are shown in Table 1.

For the volumetric compressible test, the hybrid equilibrium approach and the displacement-based one converge to the exact solution, as shown in the convergence graphs plotted in Figure 3A,B. The vertical displacement at the right side (rigid) of the Cook membrane computed by the proposed hybrid equilibrium element, with quadratic (HEE2), cubic (HEE3) and quartic stress fields (HEE4) is compared in Figure 3A with the displacement obtained by the classic displacement-based nine-node element (Q9) and is compared with the converged solution ($U_y = 21.2265$) obtained with a very fine mesh with Q9 elements. The relative error of the vertical displacement with respect to the converged solution versus the number of nodes is plotted in Figure 3B, showing the very good performance of the equilibrium-based formulation, especially for the coarse meshes. The maps of horizontal and vertical displacements obtained by the HEE and Q9 elements, with meshes of 8×12 elements, are plotted and compared in Figure 4. The nodes of the meshes are marked in the figure. In HEEs the displacement maps are plotted through a set of subdomain for each finite element and displacement is generally discontinuous at the vertices. Note that the HEE solutions are indistinguishable from one another and from the Q9 displacement-based response. The displacement discontinuities between adjacent sides are not appreciable in the maps of displacement, although the proposed formulation is based on a nonconforming element and the mesh is quite coarse.

To assess the accuracy of the present procedure the convergence analysis is also carried out in terms of the maximum principal stress in Figure 5A and in terms of relative error between the numerical solutions and the converge one ($\sigma_1 = 0.25439$ obtained with a very fine mesh with Q9 elements) in Figure 5B. The results of the HEEs with quadratic, cubic, and quartic stress fields are compared with the Q9 solution and the converged value, obtained with the extremely refined meshes of the HEE4 and Q9 solutions. The percentage relative error shown in Figure 5B highlights the excellent performance of the high-order (cubic and quartic) stress field equilibrium formulation for the stress prediction in the elastic static analysis, showing a much lower error than the Q9 solution for a comparable number of nodes of the discretization. The elastic solution of the Cook's membrane produces a stress singularity at the upper left corner with negative principal stresses, therefore the convergence test cannot be represented in terms of the minimum principal stress or in terms of the maximum tangential stress, with enhancing values at the mesh refinement.

TABLE 1 Details of the meshes analyzed for the Cook membrane problem with the hybrid equilibrium element and with the classic nine-node element

HEE2		HEE3		HEE4		Q9	
Mesh	**No. nodes**	**Mesh**	**No. nodes**	**Mesh**	**No. nodes**	**Mesh**	**No. nodes**
4×8	324	4×8	432	4×8	540	4×8	153
8×12	924	8×12	1232	8×12	1540	8×12	425
16×24	3576	16×32	6336	12×24	4500	16×24	1617
26×52	12,402	24×48	18,984	20×40	12,300	24×48	4753
26×52	28,884	40×100	48,560	20×40	25,410	40×80	13,041
50×120	54,000			36×90	48,600	80×160	51,000

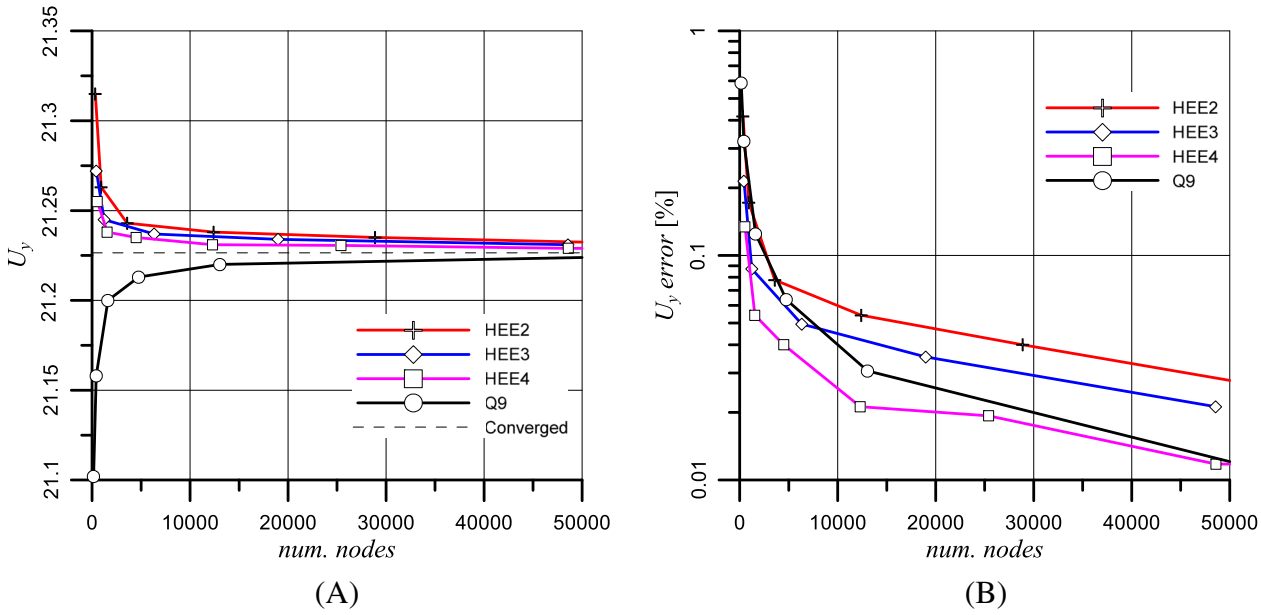

FIGURE 3 Graphic of convergence test for the compressible Cook test, in terms of (A) vertical displacement u_y at the loaded end versus number of nodes; (B) percentage error with respect to the converged solution versus number of nodes

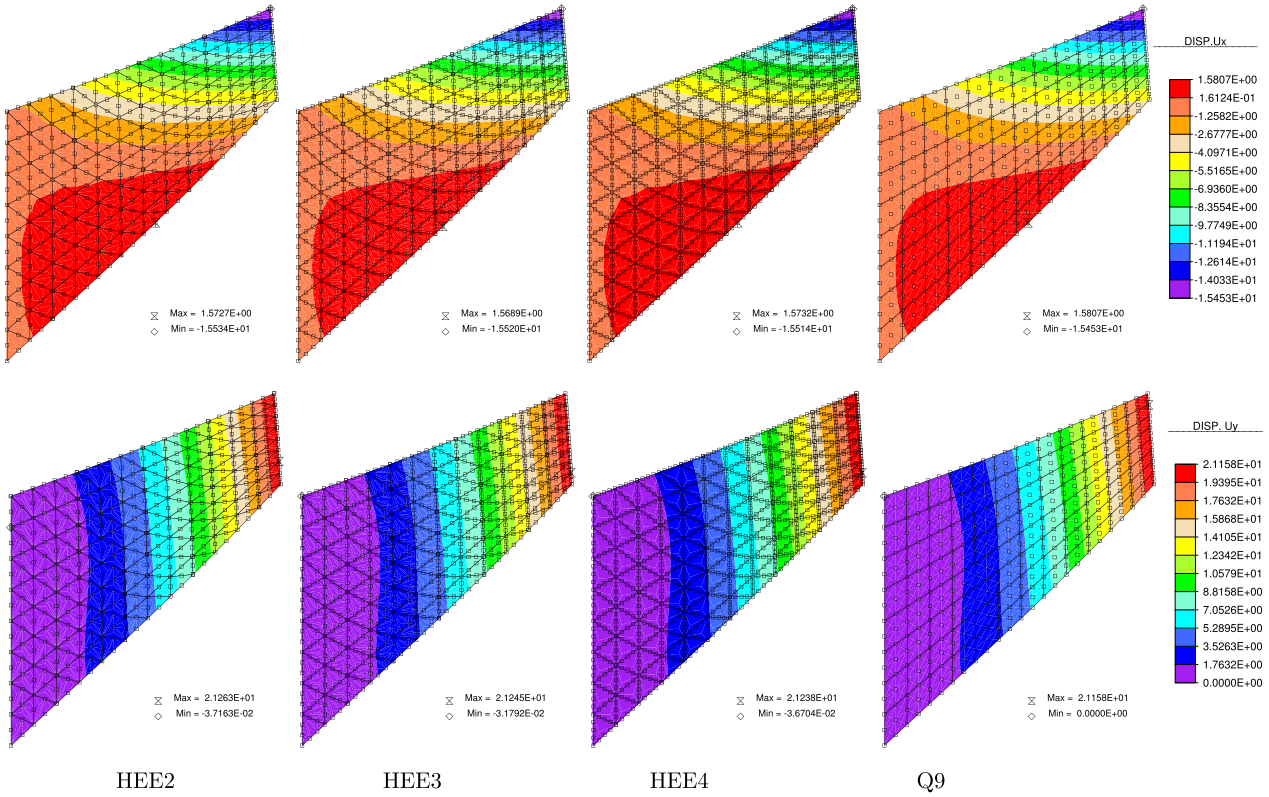

FIGURE 4 Maps of horizontal and vertical displacements of compressible the Cook membrane test, for the hybrid equilibrium element with quadratic stress field (HEE2), cubic stress field (HEE3), quartic stress field (HEE4) and for the nine-node displacement-based element (Q9), with meshes of 8×12 elements. The nodes of the meshes are marked

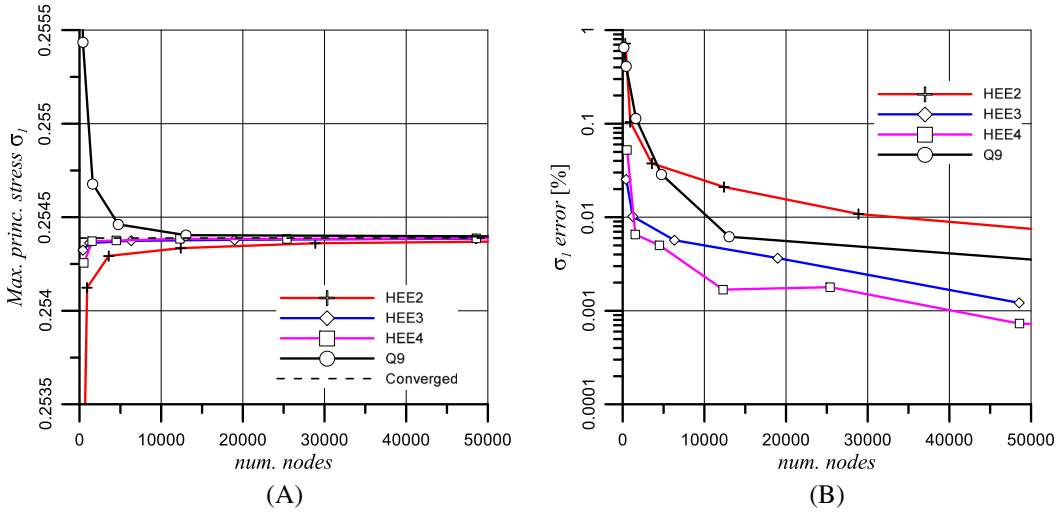

FIGURE 5 Graphic of convergence test for the compressible Cook test, in terms of (A) maximum principal stress σ_1; (B) relative error with respect to the converged solution

The elastic static response of the cook membrane problem is completed by the map of stresses, which are represented in Figure 6 in terms of the maximum principal stress, minimum principal stress, and maximum tangential stress, obtained with the HEE with quadratic stress field (HEE2), cubic stress field (HEE3), and quartic stress field (HEE4), and compared with the results obtained with the Q9 displacement-based formulation.

The accuracy of the proposed procedure is even more noticeable for the quasi-incompressible materials, for which the classic displacement-based formulation comes up against into the volumetric locking and the mixed formulations, or reduced numerical integration of the volumetric strain energy, are usually employed (see Reference 9). In terms of displacement the hybrid equilibrium approach and the displacement-based one converge to the exact solution, as shown in the convergence graphs plotted in Figure 7A,B, where the vertical displacement at the right side (rigid) of the Cook membrane, computed by the proposed hybrid equilibrium element, with quadratic (HEE2), cubic (HEE3), and quartic stress fields (HEE4) is compared with the displacement obtained by the classic DB nine-node element (Q9) and is compared with the converged solution. The converged displacement is evaluated as the mean value of the results obtained with the very fine meshes of the HEE4 and Q9 solutions. The convergence graphs in Figure 7A,B clearly show the better performance of the equilibrium formulation with respect to the displacement-based one, especially for coarse meshes. The accuracy of the HEE formulation is clear in the convergence diagram plotted in Figure 8 in terms of the maximum principal stress, showing an almost perfect convergence of the equilibrium based solution and the lack of convergence of the DB formulation. The maps of horizontal and vertical displacements obtained using the HEE and Q9 elements, with meshes of 8×12 elements, are plotted and compared in Figure 9. The HEE-solutions are almost indistinguishable from one another and from the Q9 displacement-based response and the displacement discontinuities between adjacent elements are not appreciable in Figure 9.

The convergence graphs in the Figures 3, 5, and 7 show also that the HEE formulation is a potential tool for the dual analysis and the error estimation of DB solutions. In fact, as stated in the pioneering work of Fraeijs de Veubeke[1] and more recently in References 41,42, the displacement based formulation and the equilibrium based one respectively provide a lower bound and an upper bound in the elastic solution in terms of strain energy. However, bounds of arbitrary nodal displacements or of stresses cannot be guaranteed.

The elastic static response of the cook membrane problem is completed by the map of stresses, which are represented in Figure 10 in terms of the maximum principal stress, minimum principal stress, and maximum tangential stress, obtained with the HEE with quadratic stress field (HEE2), cubic stress field (HEE3), and quartic stress field (HEE4), and with the Q9 DB formulation. The maps of principal stresses in Figure 10 make it evident the limitation of the classic DB formulation for analysis of nearly incompressible elastic material, with inconsistent stress distributions and with non-converging solution in terms of stress. Such a problem affects the volumetric stress, therefore and the shear stress is less influenced. The HEE formulation is completely free of any volumetric locking numerical problem for all the considered stress orders.

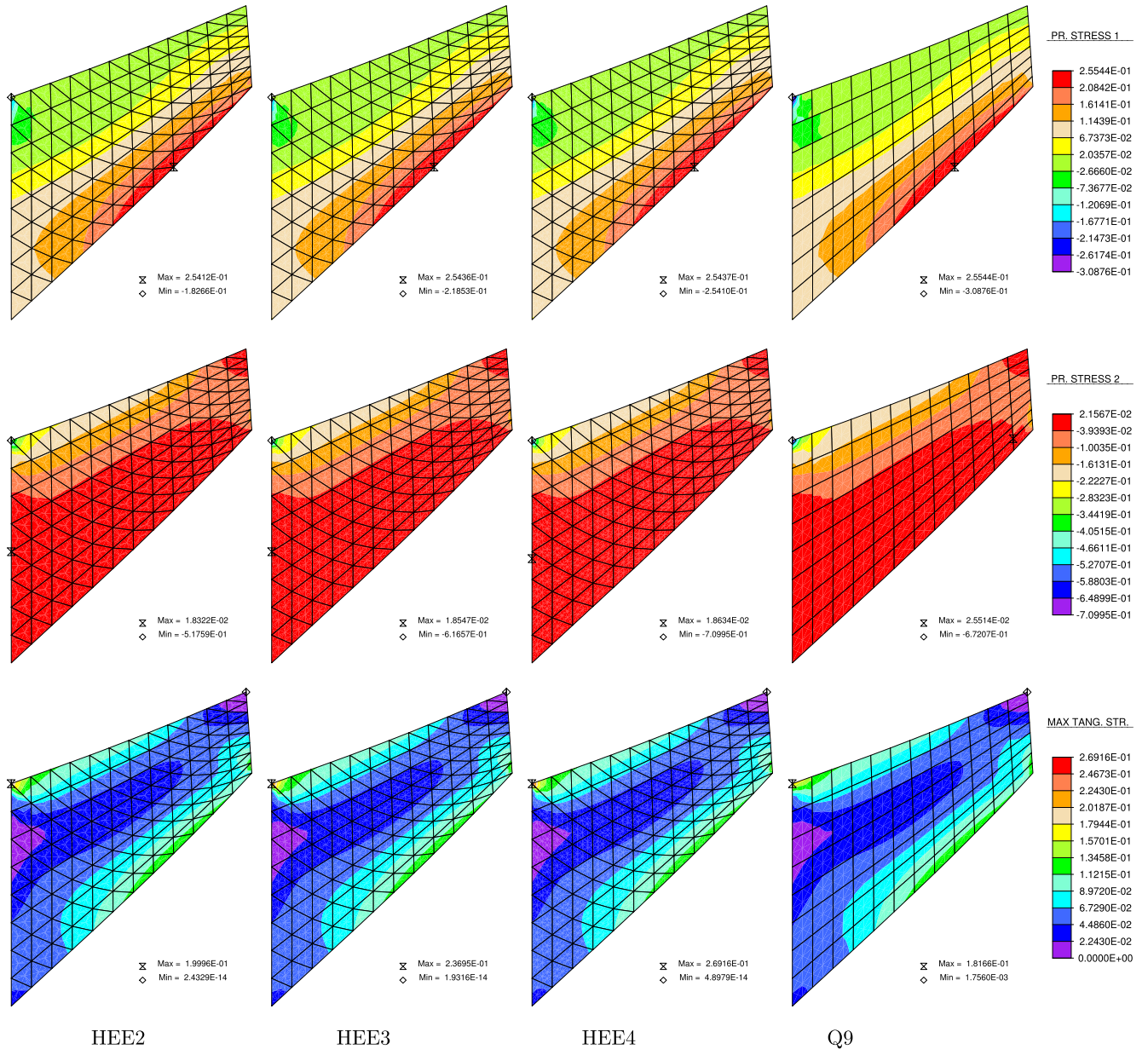

FIGURE 6 Maps of principal stresses and maximum tangential stress of compressible Cook membrane test, for the hybrid equilibrium element with quadratic stress field (HEE2), cubic stress field (HEE3), quartic stress field (HEE4) and for the nine-node displacement-based element (Q9), with meshes of 8×12 elements

4.2 | The elastic dynamic problem of a cantilever beam

The accuracy of the high-order stress fields in the proposed formulation is tested under dynamic conditions for a simple cantilever beam subjected to a dynamic pulse. The problem is analyzed in Reference 28 with the left side fixed and with two different load setting: the axial and shear uniform pressures $p_n = p_t = 1$ applied at the free end.

The uniform shear stress at the right end does not satisfy the local equilibrium condition at the two corners and intrinsically conflict with the proposed equilibrium formulation. Therefore, in the present article the shear load is applied as a quadratic tangential traction with null values at the two corners and maximum value $p_t = 1.5$ at point B represented in Figure 11, according to the Jourawsky beam solution and with unitary tangential force ($\int_{-h/2}^{h/2} p_t dy = 1$), with $h = 1$ mm the beam thickness. Finally, a third load condition is applied in terms of a uniform vertical body force b_y with a plane strain quasi-incompressible condition.

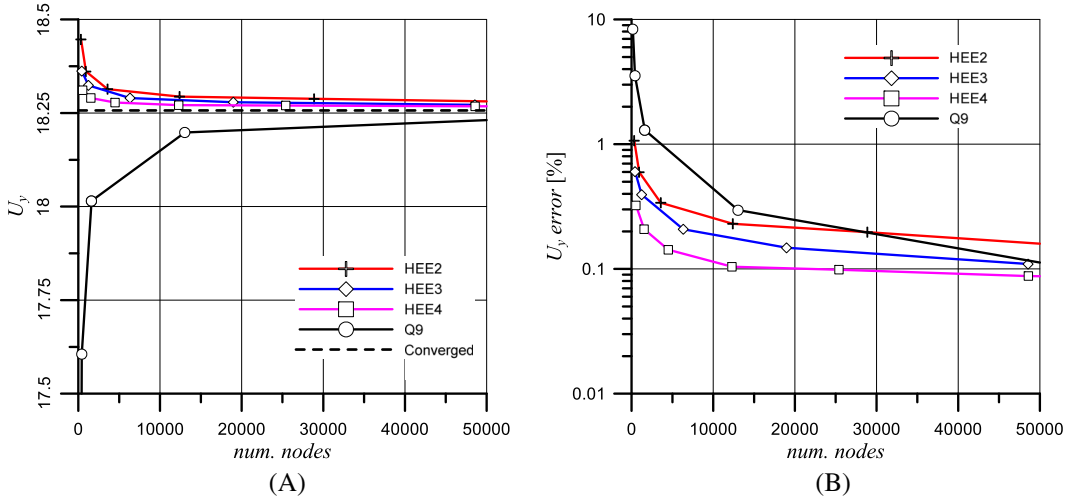

FIGURE 7 Graphic of convergence test for the quasi-incompressible Cook test, in terms of (A) vertical displacement u_y at the loaded end versus the number of nodes; (B) relative error with respect to the converged solution versus the number of nodes

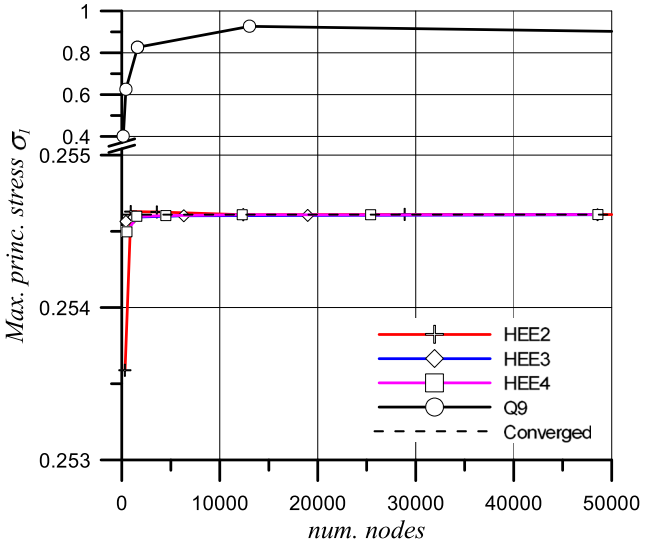

FIGURE 8 Graphic of convergence test for the quasi-incompressible Cook test, in terms of maximum principal stress σ_1 versus the number of nodes

The sizes of the cantilever beam and the three loading setting are represented in Figure 11. The material properties are the following: elastic modulus $E = 200$, Poisson ratio $\nu = 0.33$, and mass density $\rho = 0.785$. For the quasi-incompressible material the Poisson ratio is $\nu = 0.4999$. The dynamic pulse load is applied by the time continuous loading law $f_1(t)$ represented in Figure 11, with two values of the pulse load application time: $\Delta T_1 = 8$ s and $\Delta T_2 = 0.08$ s. The body force $f_1(t)b_y$ is applied only with the first impulse loading law, that is $\Delta T_1 = 8$ s. The dynamic pulse load is also applied by the time discontinuous loading law $f_2(t)$ with pulse application time: $\Delta T = 4$ s.

The dynamic analyses were performed with the DB nine-node element (Q9) and with the proposed dynamic HEE formulation with quadratic, cubic, and quartic stress fields. Two different meshes were considered: the 2×20 coarse mesh and the 10×100 fine mesh. The Q9 fine mesh was defined by 16×160 nine-node elements. The coarse meshes and the fine meshes are represented together with the displacement map in Figure 15 and with the map of normal stress in Figure 16. The number of nodes of the meshes is shown in Table 2. For the proposed meshes, the HEE formulation produces a spurious kinematic mode at the corner A which is restrained by a rigid link between the horizontal degrees of freedom of the two coincident nodes at the corner A (see Reference 18 for details).

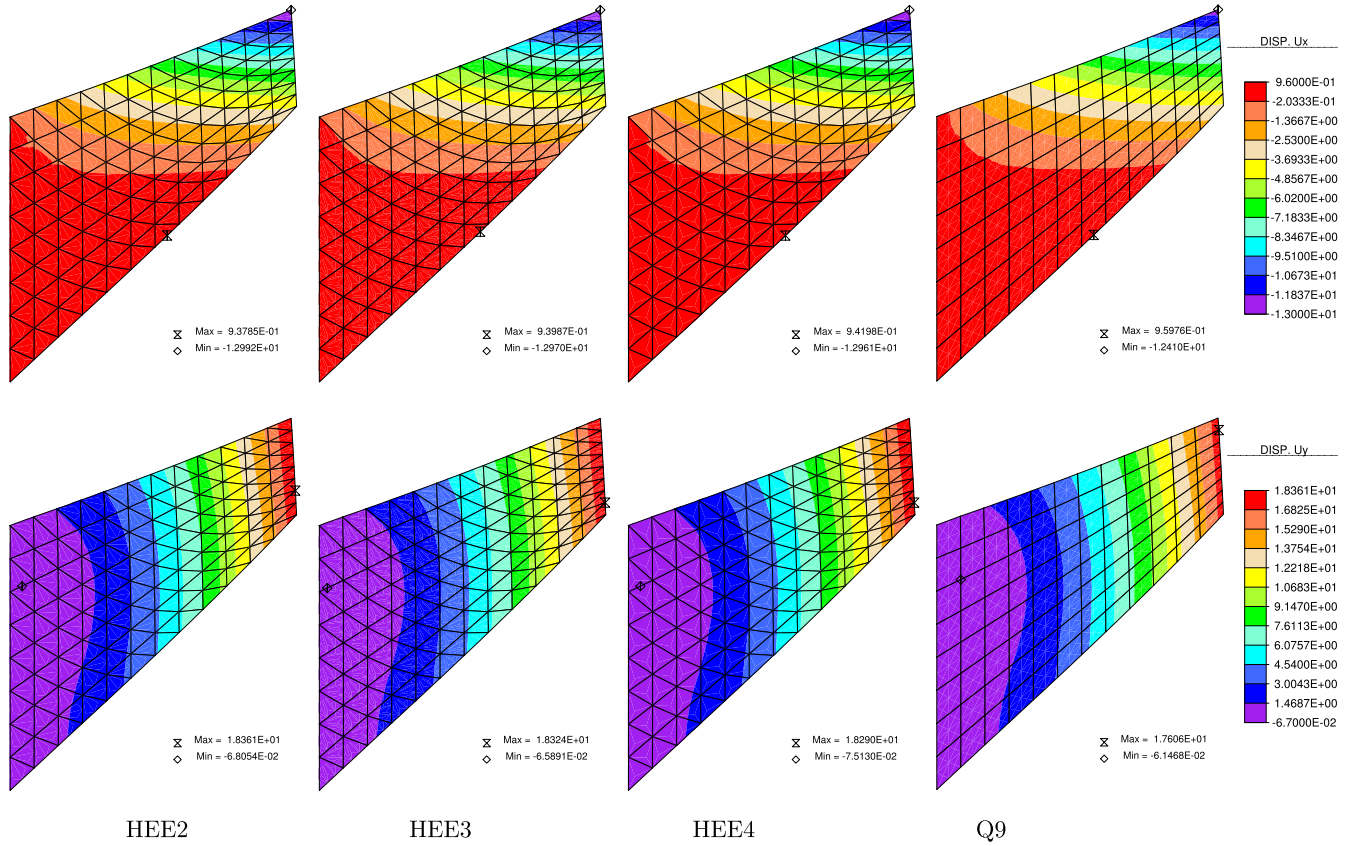

FIGURE 9 Maps of horizontal and vertical displacement of the quasi-incompressible Cook membrane test, for the hybrid equilibrium element with quadratic stress field (HEE2), cubic stress field (HEE3), quartic stress field (HEE4) and for the nine-node displacement-based element (Q9), with meshes of 8×12 elements

4.2.1 | Slow axial pulse load

The numerical simulation of elastic-dynamic analysis of the cantilever beam subjected to the uniform axial load $\boldsymbol{p}_n$ is applied by the time continuous loading law $f_1(t)$ represented in Figure 11, with the greater value of pulse load application time: $\Delta T_1 = 8$ s, with constant time increment $\Delta t = \Delta T_1/160 = 5 \cdot 10^{-2}$ s and with $t_{max} = 50$ s.

The results of the dynamic analysis obtained with the coarse meshes of the dynamic HEE formulation and with the standard DB one, are compared in Figure 12A in terms of horizontal and vertical displacements and in terms of normal stress σ_x, at point B represented in Figure 12B. The four different solutions (HHE2, HEE3, HEE4, and Q9) are practically coincident in terms of horizontal displacement u_x at point B, whereas some small differences can be observed in terms of the vertical component u_y, especially in the HEE2 formulation. This error is probably due to the asymmetry of the HEE meshes. Conversely, the HEE formulation computes the exact value of the normal stress σ_x at point B, which is imposed as a boundary condition, and the DB formulation produces non null stress values after the pulse load, when the right end is unloaded and null normal stress is expected. The differences between the HEE and DB formulations are very small and vanish completely with the fine meshes, so that it can be stated that the two formulations converge to the exact elastic dynamic solution.

4.2.2 | Fast axial pulse load

The differences between the two formulations are more pronounced for the faster pulse load, which is defined by the continuous loading law $\boldsymbol{p}_n f_1(t)$ with $\Delta T = 0.08$ s, with constant time increment $\Delta t = \Delta T_2/160 = 5 \cdot 10^{-4}$ s and with $t_{max} = 0.50$ s. The relevant numerical results, obtained with coarse and fine meshes, with the quadratic, cubic, and quartic HEE

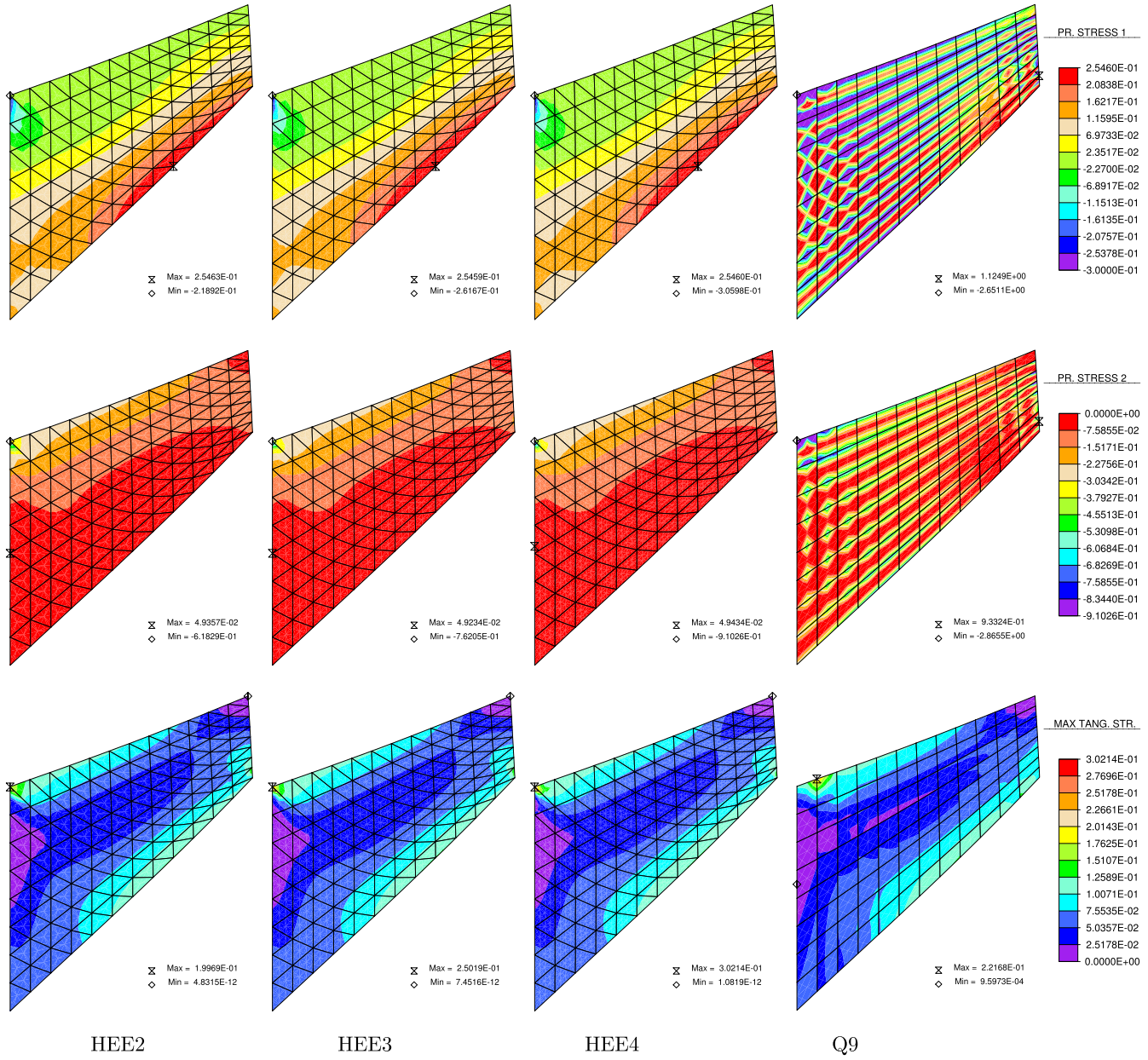

FIGURE 10 Maps of principal stresses and maximum tangential stress of quasi-incompressible Cook membrane test, for the hybrid equilibrium element with quadratic stress field (HEE2), cubic stress field (HEE3), quartic stress field (HEE4) and for the nine-node displacement-based element (Q9), with meshes of 8×12 elements

formulations and with the DB one are compared in Figure 13 in terms of horizontal and vertical displacement components at point A in the time domain.

The numerical solutions are also compared in Figure 14A–D in terms of evolution of stress components at point B in the time domain. The stress components σ_x and τ_{xy} are imposed as a boundary condition in the HEE formulations and coincide to the exact solutions for both coarse meshes and fine meshes. The DB solution provides some small errors in terms of stress which become negligible with the fine mesh. Finally, the evolution in the time domain of normal stress σ_y, which is not imposed as a boundary condition in HEE formulation, is plotted in Figure 14B for the coarse mesh, with some differences between the different solutions, and in Figure 14D for the fine mesh, showing perfectly coincident results and convergence of the two formulations to the exact solution. In this sense, the proposed dynamic equilibrium-based formulation can also be considered as a dual approach for the error estimation and for the convergence analysis of the classic DB approach.

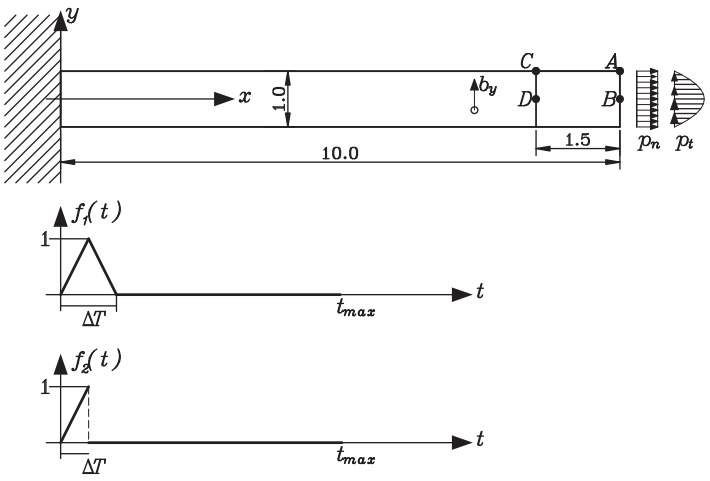

FIGURE 11 The cantilever beam dynamic test with the three load setting: the axial uniform pressure $\boldsymbol{p}_n$, the quadratic tangential pressure $\boldsymbol{p}_t$, and the vertical body force b_y. The loads are applied as dynamic pulse by the continuous loading law $f_1(t)$ and the discontinuous loading law $f_2(t)$

TABLE 2 Details of the discretizations employed in the dynamic analysis of the cantilever beam, with the hybrid equilibrium element and with the DB nine-nodes element

HEE2		HEE3		HEE4		Q9	
Mesh	**No. nodes**	**Mesh**	**No. nodes**	**Mesh**	**No. nodes**	**Mesh**	**No. nodes**
2×20	426	2×20	568	2×20	710	2×20	205
10×100	9330	10×100	12,440	10×100	15,550	16×160	10,593

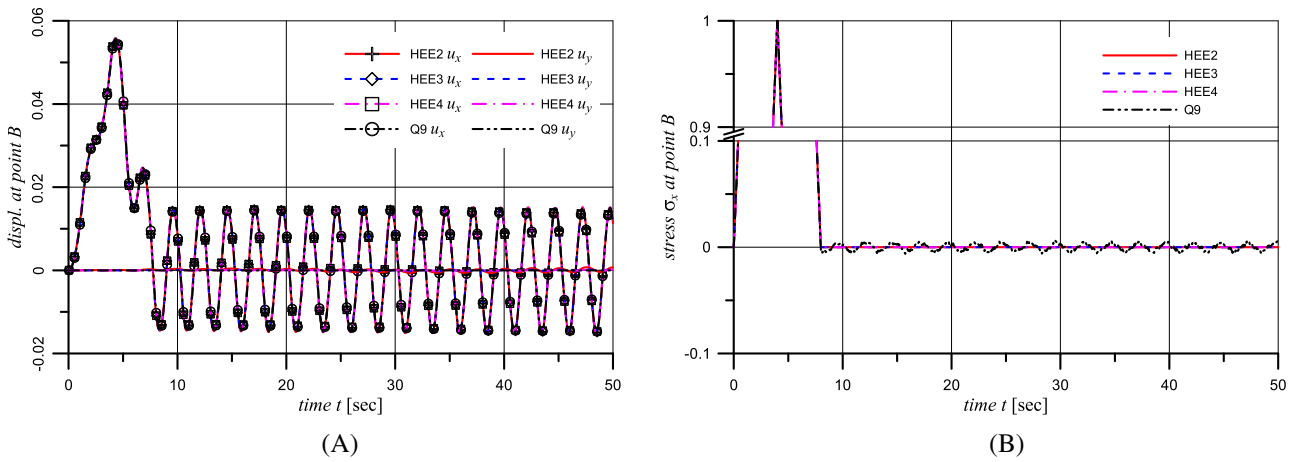

FIGURE 12 Dynamic response of a cantilever beam subjected to a slow pulse axial load $\boldsymbol{p}_n f_1(t)$ ($\Delta T = 8$ s), for the quadratic, cubic, and quartic HEEs and for the nine-node DB element, with coarse 2×10 meshes, in terms of (A) horizontal and vertical displacement at point B; (B) normal stress σ_x at point B

The maps of horizontal displacement u_x and the maps of normal stress σ_x, at time $t = 16.0$ s, computed with the HEE formulation and the DB approach with coarse and fine meshes are plotted respectively in Figures 15 and 16. There it can be observed that displacement and stress computed with the coarse meshes do not coincide with each other and the equilibrium-based solutions do not show a symmetric response, due to the asymmetry of the HEE meshes. Moreover, some displacement discontinuity between coincident nodes is noticeable in the solution with quadratic stress fields (HEE2) but vanishes altogether with higher stress fields (HEE3 and HEE4). The numerical results for the fine meshes respect the symmetry condition of the axial load and are all perfectly coincident in terms of both displacement and stress,

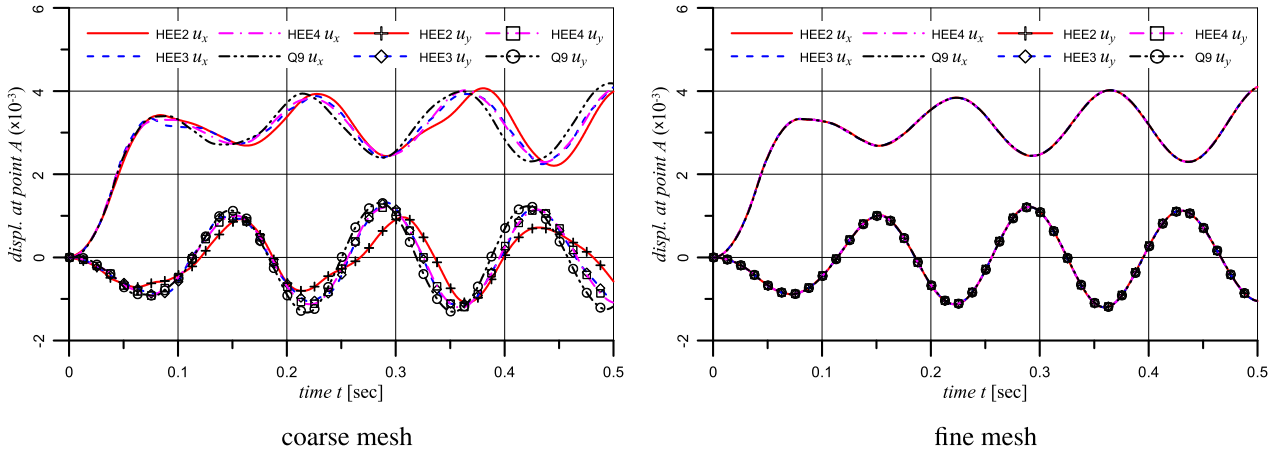

FIGURE 13 Dynamic response of a cantilever beam subjected to the fast axial pulse load $\boldsymbol{p}_n f_1(t)$ ($\Delta T = 0.08$ s), in terms of vertical and horizontal displacement at point A, for the quadratic, cubic, and quartic HEE and for the nine-node DB element

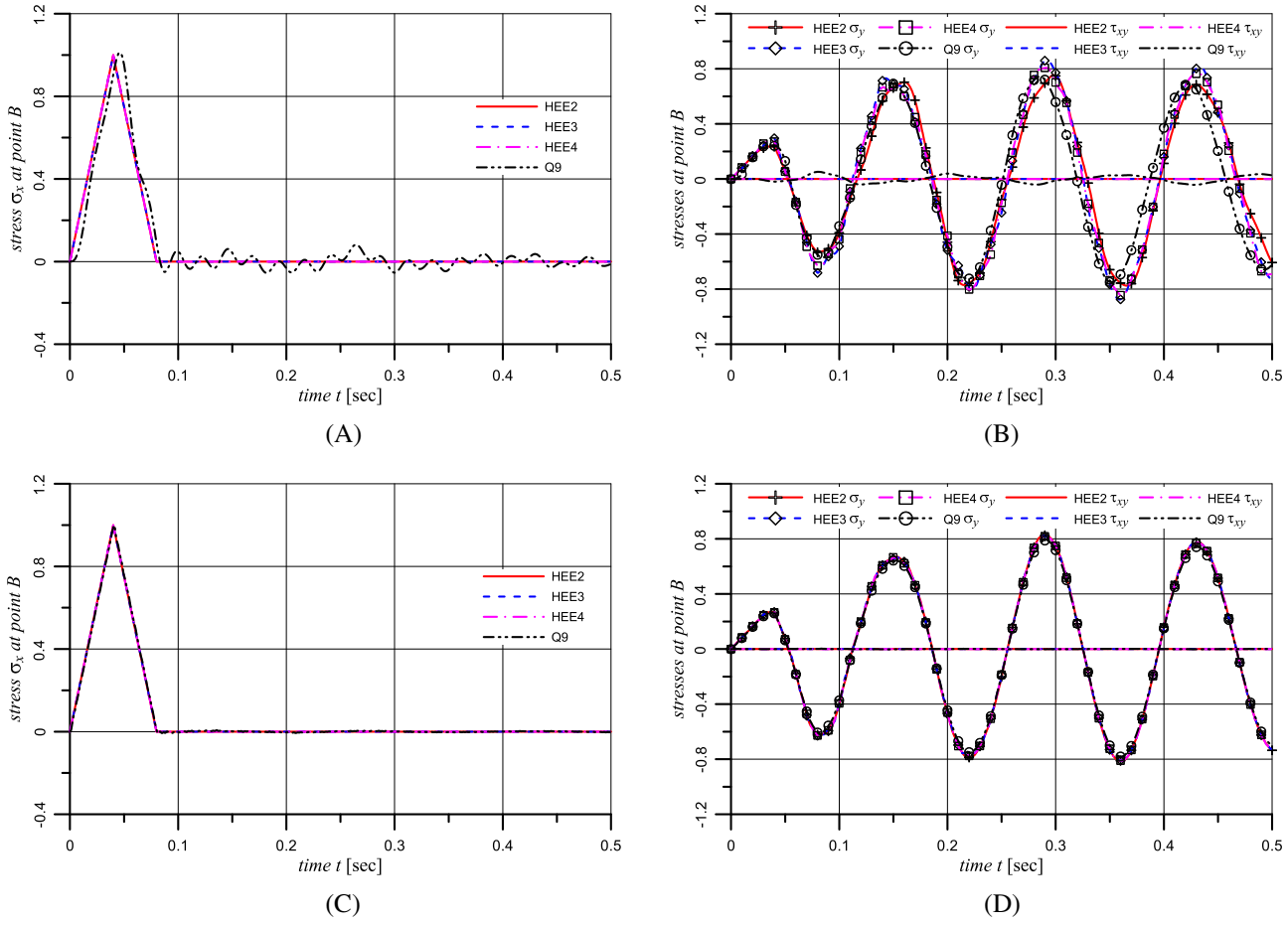

FIGURE 14 Dynamic response of a cantilever beam subjected to the fast pulse axial load $\boldsymbol{p}_n f_1(t)$ ($\Delta T = 0.08$ s), at point B in terms of (A) normal stress σ_x with coarse mesh; (B) normal stress σ_y and tangential stress τ_{xy} with coarse mesh; (C) normal stress σ_x with fine mesh; (D) normal stress σ_y and tangential stress τ_{xy} with fine mesh

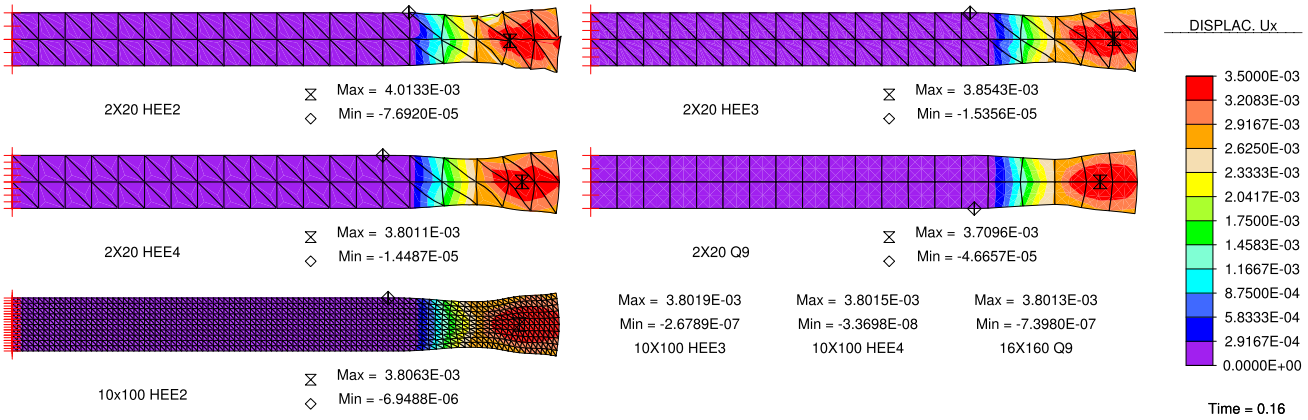

FIGURE 15 Map of horizontal displacement u_x at time $t = 0.16$ s for the cantilever beam subjected to the fast pulse axial load $\boldsymbol{p}_n f_1(t)$ ($\Delta T = 0.08$ s), computed with the quadratic, cubic, and quartic HEE and with the nine-node DB element

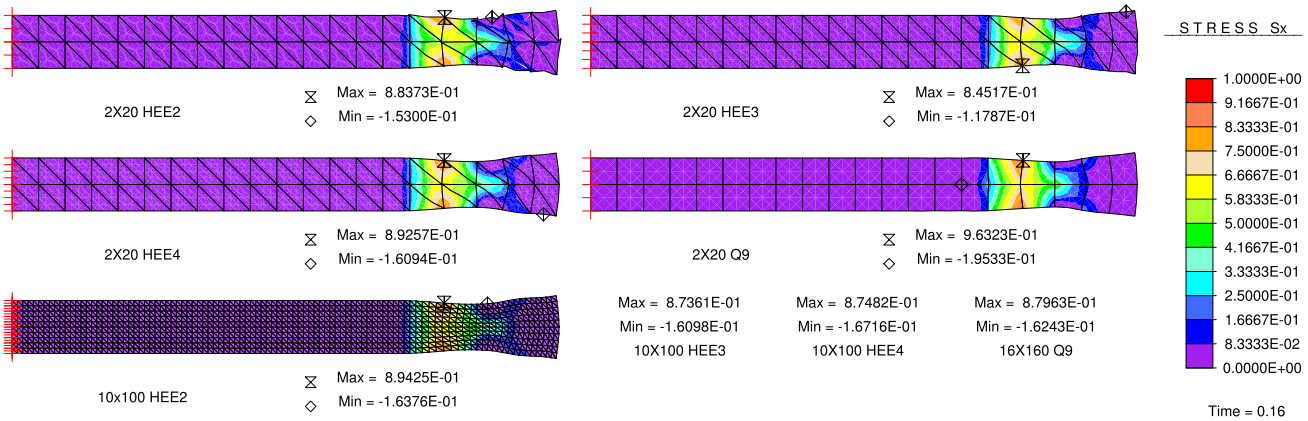

FIGURE 16 Map of normal stress σ_x at time $t = 0.16$ s for the cantilever beam subjected to the fast pulse axial load $\boldsymbol{p}_n f_1(t)$ ($\Delta T = 0.08$ s), computed with the quadratic, cubic, and quartic HEE and with the nine-node DB element

confirming the convergence of the proposed formulation and the DB approach to the exact solution. The maps of stress and displacement of the fine mesh solutions are plotted for the quadratic HEE formulation (HEE2), whereas only maximum and minimum values are reported for the other solutions, both for this numerical simulation and for the following ones.

4.2.3 | Slow tangential pulse load

Good performances of the hybrid dynamic equilibrium formulation are also found in the numerical simulation of the cantilever beam subjected to a slow and continuous pulse tangential load $\boldsymbol{p}_t f_1(t)$, with the greater value of pulse load application time: $\Delta T_1 = 8$ s, with constant time increment $\Delta t = \Delta T_1/160 = 5 \cdot 10^{-2}$ s and with $t_{max} = 50$ s. The results computed with coarse meshes are plotted in the two graphs in Figure 17 in terms of vertical displacement u_y at point A and in terms of horizontal displacement u_x at points A and B, showing negligible differences between the equilibrium-based solutions and the displacement-based one. The numerical results are also plotted in the two graphs in Figure 18 in terms of tangential stress τ_{xy} at corner A, where the exact solution is null in the whole time domain, and at point B where the quadratic tangential load imposes the stress value $\tau_{xy} = 1.5$.

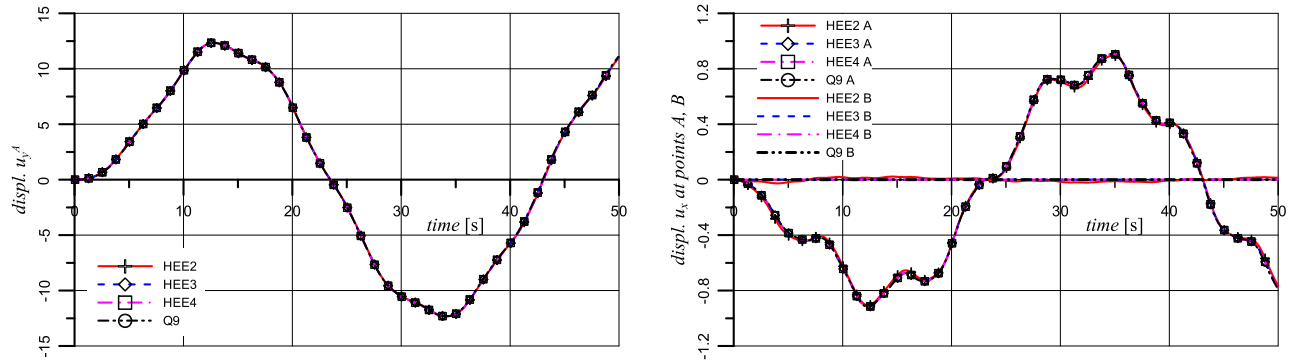

FIGURE 17 Dynamic response of a cantilever beam subjected to a slow tangential pulse load $\boldsymbol{p}_t f_1(t)$ ($\Delta T = 8$ s), in terms of vertical displacement u_y at point A, and in terms of horizontal displacement u_x at points A and B, for the quadratic, cubic, and quartic HEEs and for the nine-node DB element, with coarse 2×20 meshes

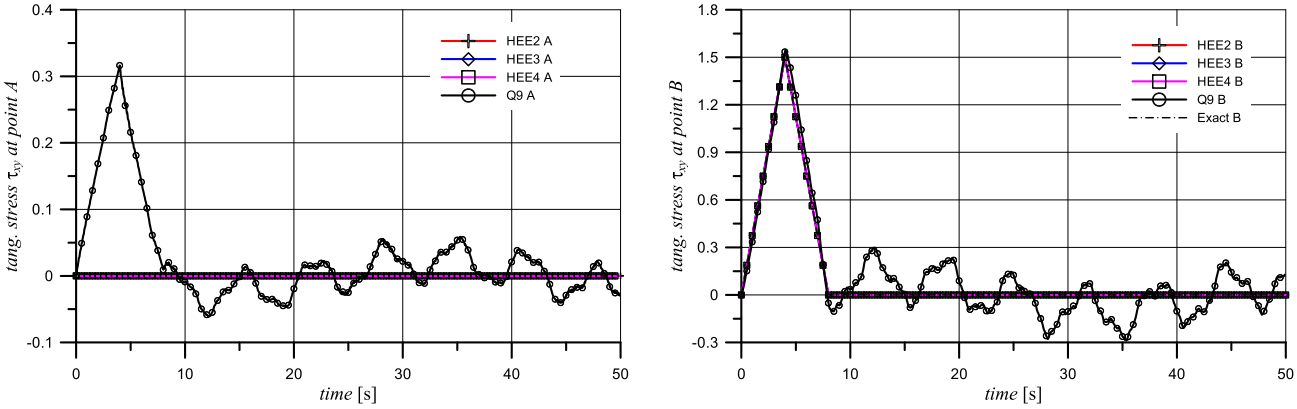

FIGURE 18 Dynamic response of a cantilever beam subjected to a slow tangential pulse load $\boldsymbol{p}_t f_1(t)$ ($\Delta T = 8$ s), in terms of tangential stress τ_{xy} at points A and B, for the quadratic, cubic, and quartic HEEs and for the nine-node DB element, with the coarse 2×10 meshes

The numerical results for a cantilever subjected to a slow pulse tangential load confirms the good results of the proposed formulation, showing some slightly incorrect values of displacement u_x at point B computed with the quadratic equilibrium formulation (HEE2). The cubic and quartic stress field equilibrium formulations produce exact values. By contrast, the equilibrium-based approach produces exact values of stresses at the free end, where tangential stress is applied as a boundary condition, and the DB solution computes incorrect values of the tangential stress for all time steps. The distribution of the three stress components at the right end at time step $t = 4$ s, computed with the coarse meshes of quadratic, cubic, and quartic equilibrium elements and with nine-node DB elements, are plotted in Figure 19. This graph clearly shows the limits of the classical DB models in stress response: linear tangential stress instead of quadratic trend; nonzero normal stress σ_x at the free end; and nonzero normal stress σ_y at the two corners. The differences between the three equilibrium formulation are due to the high order of the exact solution, which is defined by a cubic function for the normal stress component σ_y. So the quadratic formulation can reproduce only an approximate solution, whereas the cubic formulation and the quartic one can reproduce the exact solution. The numerical results are accompanied by maps of the vertical displacement and maps of the tangential stress at time step $t = 16$ s plotted respectively in Figures 20 and 21, which were computed with the four considered formulations using coarse and fine meshes.

4.2.4 | Fast tangential pulse load

Similarly to the case of axial force, the differences between the equilibrium-based and displacement-based formulations are more pronounced for the faster tangential pulse load, which is defined by the pulse tangential load $\boldsymbol{p}_t f_1(t)$, with

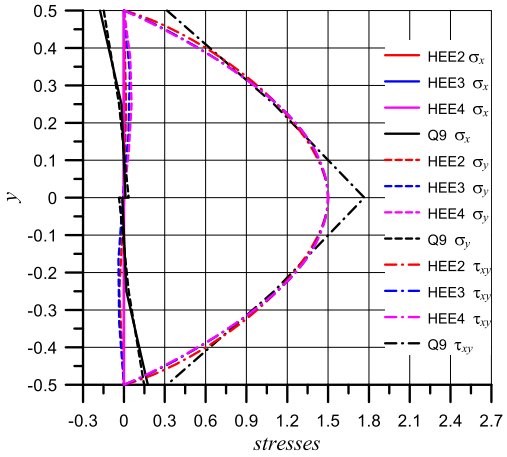

FIGURE 19 Distribution of the stress components at the right end of the cantilever beam at the step $t = 4$ s, for the quadratic, cubic, and quartic HEEs and for the nine-node DB element, with coarse 2×10 meshes

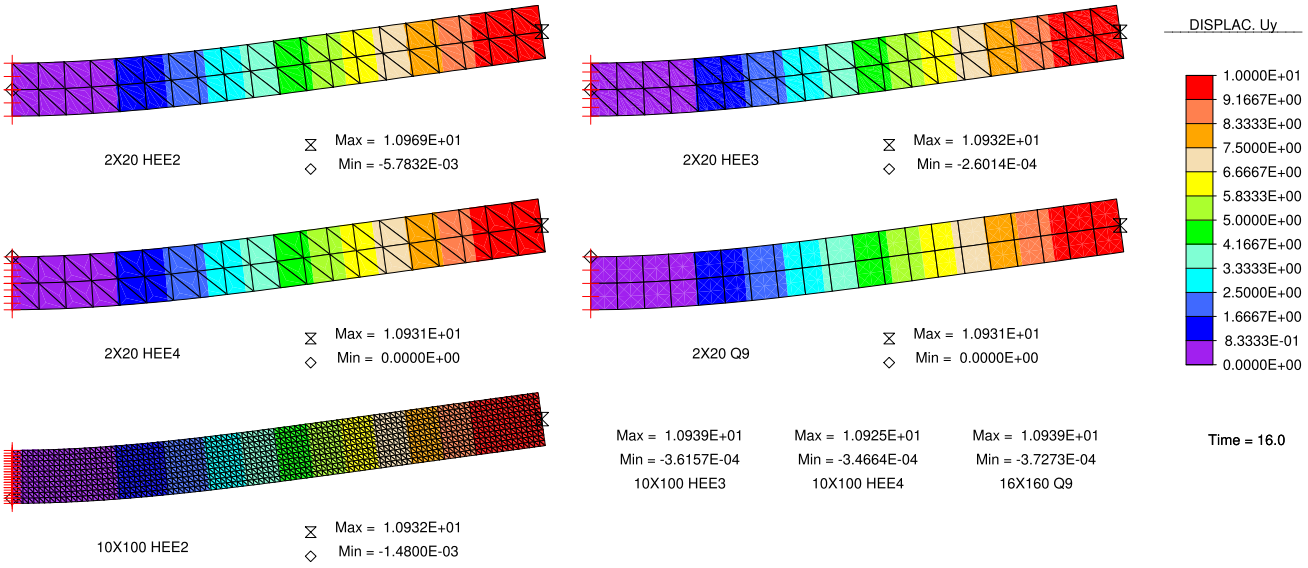

FIGURE 20 Map of vertical displacement u_y at time $t = 16$ s for a cantilever beam subjected to the slow tangential pulse load $\boldsymbol{p}_t f_1(t)$ ($\Delta T = 8$ s), computed with the quadratic, cubic, and quartic HEEs and with the nine-node DB element

the value of pulse load application time $\Delta T_2 = 0.08$ s, with constant time increment $\Delta t = \Delta T_2/160 = 5 \cdot 10^{-4}$ s and with $t_{max} = 0.5$ s. The numerical results computed with the coarse meshes are compared in the first graph in Figure 22 in terms of vertical and horizontal displacement components u_x and u_y at point A in the whole time domain, showing significant differences between the four formulations with coarse meshes, especially for the quadratic equilibrium-based one (HEE2). This differences completely disappear with fine meshes, as shown in the second graph in Figure 22, confirming the convergence of the proposed formulation to the exact solution.

The numerical results computed with coarse meshes are compared in the first graph in Figure 23 in terms of normal stress σ_x in the whole time domain at point C, where such component cannot be imposed as a boundary condition. In the same graph the stress components σ_y and τ_{xy} computed at point C with the Q9 DB approach are plotted. These stresses should be null, being components of the traction at the free boundary, whereas they are exactly computed by the equilibrium formulation. The same stress components are plotted in the second graph in Figure 23 for fine meshes, showing the convergence of the four formulations to the same solution, although some residual error can be observed in the stress components σ_y and τ_{xy} computed with the DB nine-node element.

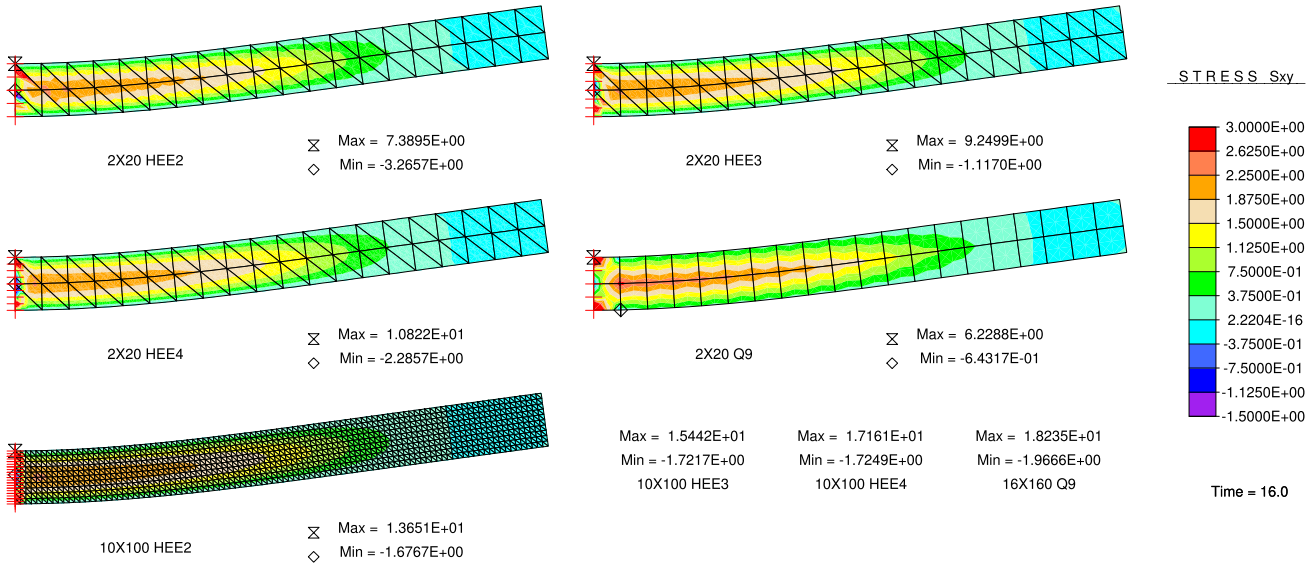

FIGURE 21 Map of tangential stress τ_{xy} at time $t = 16$ s for the cantilever beam subjected to slow tangential pulse load $\boldsymbol{p}_t f_1(t)$ ($\Delta T = 8$ s), computed with the quadratic, cubic, and quartic HEE and with the nine-node DB element

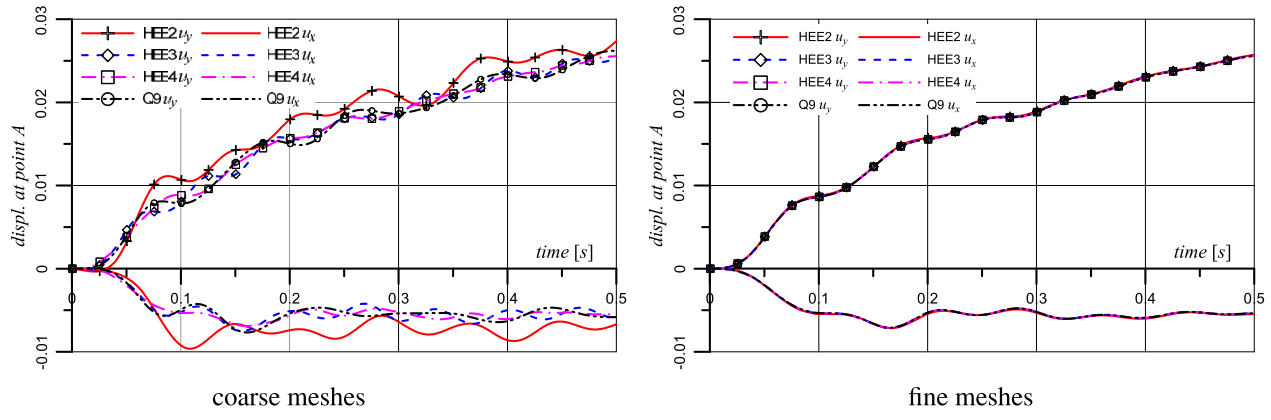

FIGURE 22 Dynamic response of a cantilever beam subjected to the fast tangential pulse load $\boldsymbol{p}_t f_1(t)$ ($\Delta T_2 = 0.08$ s) in terms of vertical and horizontal displacements u_x and u_y at point A, for the quadratic, cubic, and quartic HEEs and for the nine-node DB element

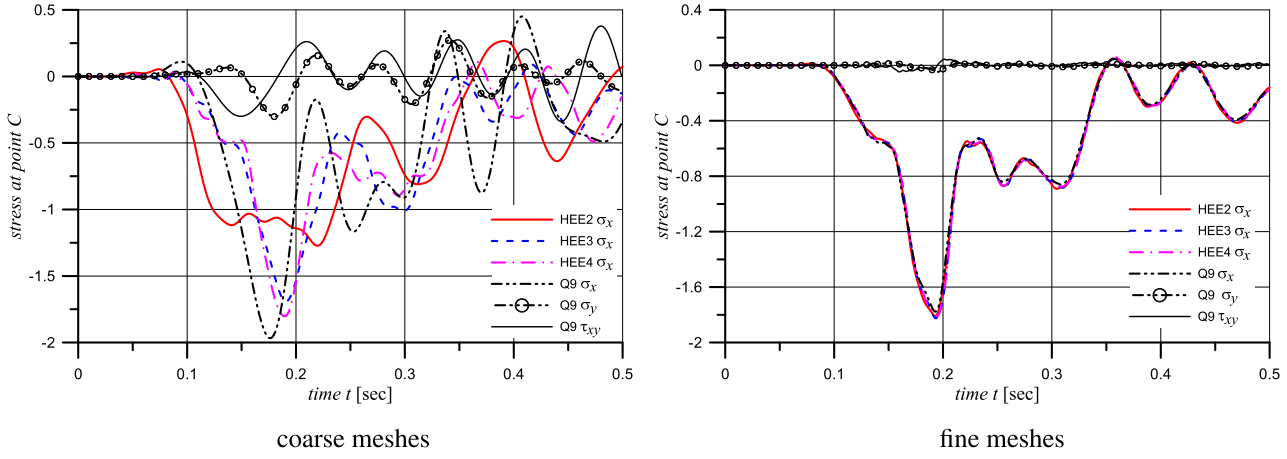

FIGURE 23 Dynamic response of a cantilever beam subjected to the fast tangential pulse load $\boldsymbol{p}_t f_1(t)$ ($\Delta T = 0.08$ s), in terms of stress components at point C for the quadratic, with the coarse and fine meshes

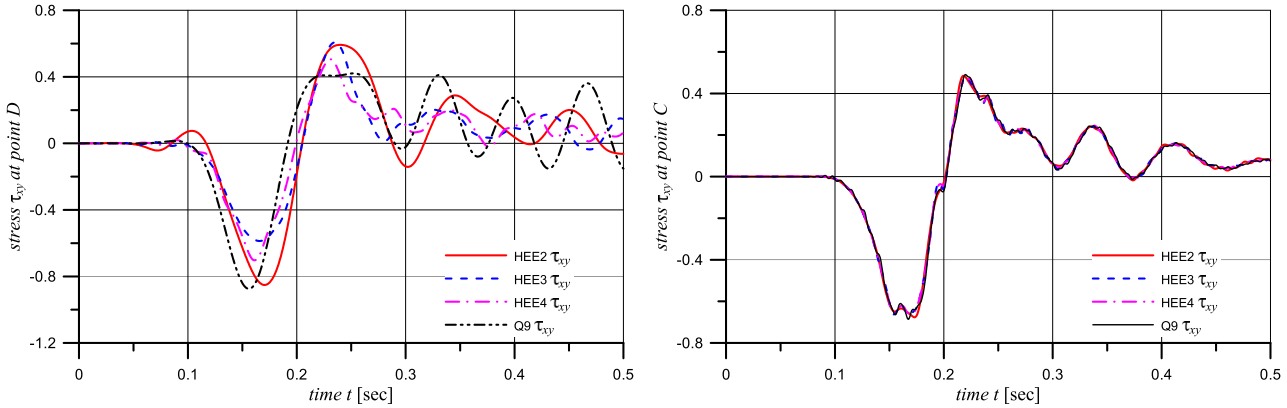

FIGURE 24 Dynamic response of a cantilever beam subjected to the fast tangential pulse load $\boldsymbol{p}_t f_1(t)$ ($\Delta T = 0.08$ s), in terms of stress components at point D, with the coarse and fine meshes

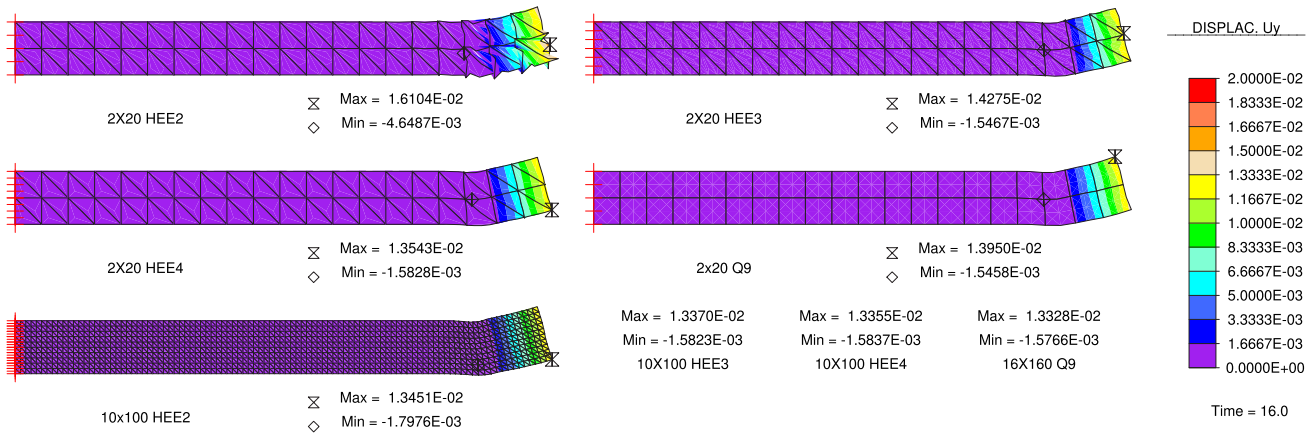

FIGURE 25 Map of vertical displacement u_y at time $t = 0.16$ s for a cantilever beam subjected to the fast tangential pulse load $\boldsymbol{p}_t f_1(t)$ ($\Delta T = 0.08$ s), computed with the quadratic, cubic, and quartic HEEs and with the nine-node DB element

The trend of tangential stress τ_{xy} in the whole time domain at the internal point D, therefore not assumed as boundary condition, is plotted in the graph in Figure 24 for the coarse meshes and for the fine meshes.

The maps of vertical displacement u_y and the maps of tangential stress τ_{xy}, at time $t = 0.16$ s, computed with the HEE formulations and the DB one, with coarse and fine meshes, are plotted respectively in Figures 25 and 26. There it can be observed that some displacement discontinuity between coincident nodes is noticeable in the solution with coarse mesh and quadratic stress field (HEE2) but totally vanishes with the higher stress fields (HEE3 and HEE4) and also with fine meshes.

In order to analyze the numerical error introduced by the Newmark time integration, the numerical simulation of the cantilever beam subjected to the fast tangential pulse load is also performed with a greater time step value $dt = \Delta T_2/16 = 5 \cdot 10^{-3}$ s and with the same time domain with $t_{max} = 0.5$ s. The differences in the numerical solutions due to the greater time step are negligible with the fine meshes both for the HEE formulation and for the DB one. The greater time step does not produces any significant error neither with the coarse meshes and with comparable effects between the HEE formulation and the DB one. For the coarse meshes, the results of the numerical simulations performed with the two different values of the time step are compared in Figure 27A in terms of tangential stress at point D, and are compared in Figure 27B in terms of vertical displacement at the point A. Figure 27A,B shows that increasing the time step with the Newmark time integration method seems to produce similar effects in the HEE formulation and in the displacement based one, that is a delay in the response with an increase of the period.

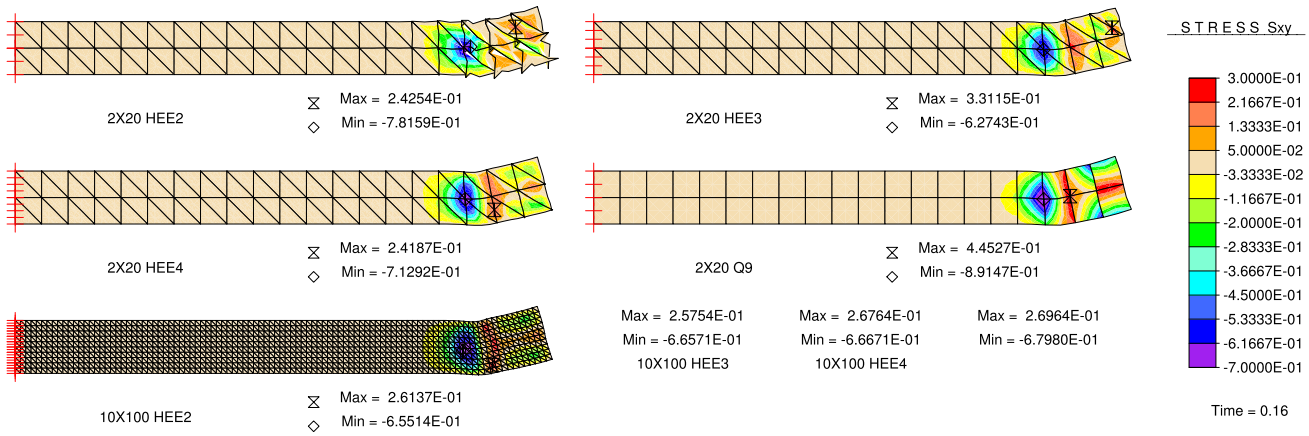

FIGURE 26 Map of tangential stress τ_{xy} at time $t = 0.16$ s for a cantilever beam subjected to the fast tangential pulse load $\boldsymbol{p}_t f_1(t)$ ($\Delta T = 0.08$ s)

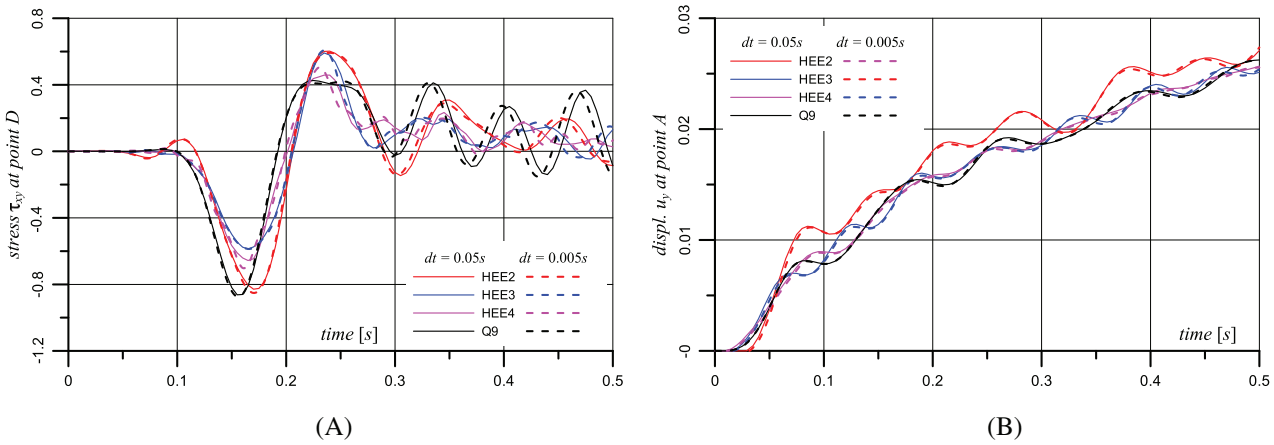

FIGURE 27 Dynamic response of a cantilever beam subjected to the fast tangential pulse load $\boldsymbol{p}_t f_1(t)$ ($\Delta T = 0.08$ s). The numerical results obtained with two different time steps ($dt = 0.05$ s and $dt = 0.005$ s) are compared in terms of (A) tangential stress τ_{xy} at point D; (B) vertical displacement at point A

4.2.5 | Slow and discontinuous tangential pulse load

The proposed hybrid equilibrium formulation and the classic DB one are also compared for the elastic-dynamic analysis of the beam cantilever subjected to the time discontinuous load, that is the tangential load $\boldsymbol{p}_t$ with the time discontinuous load function $f_2(t)$, with the value of pulse load time $\Delta T = \Delta T_1/2 = 4.0$ s and with $t_{max} = 20s$. The load discontinuity is applied in a single load step and two values of the constant time increment are considered: the standard value $dt = 0.05$ s and the very small value (compared with load application time ΔT) $dt = 0.001$ s, with a stronger discontinuity in the load time law.

The numerical results computed with the coarse meshes are plotted in the Figure 28A,B in terms of horizontal and vertical displacement u_x and u_y at point A. The results are also compared with the solution of the continuous tangential load, from which the responses diverge after the load discontinuity, and are compared with the solutions of the quadratic equilibrium formulation performed with the small time increment $dt = 0.001$ s, showing almost identical results. The numerical solutions of the discontinuous tangential load performed with the standard time increment $dt = 0.05$ s are plotted the Figure 29A in terms of tangential stress τ_{xy} at the boundary point B, showing an exact response at the load discontinuity for the HEE formulations and the approximate solution of the DB one. The tangential stress τ_{xy} at the internal

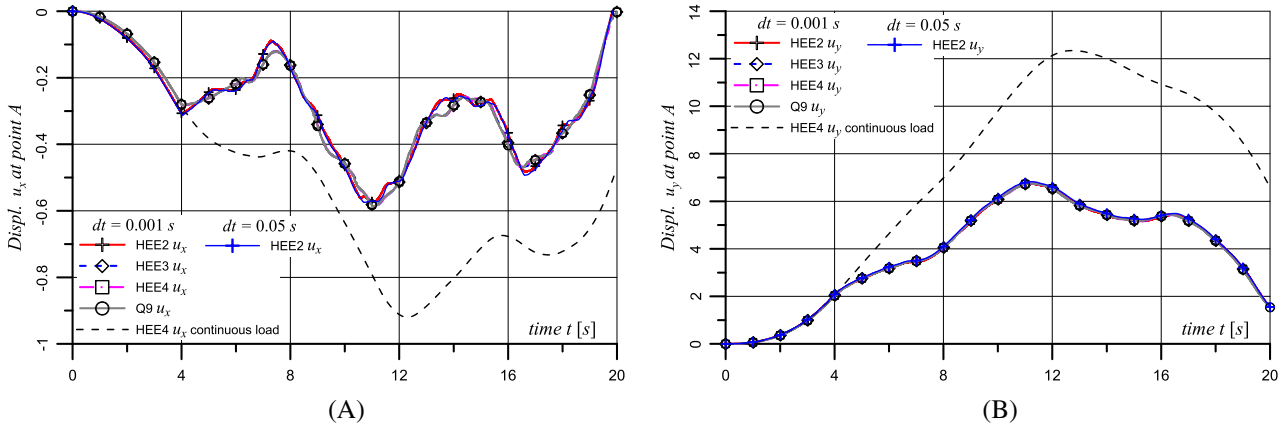

FIGURE 28 Dynamic response of a cantilever beam subjected to a discontinuous pulse tangential load $\boldsymbol{p}_t f_2(t)$ ($\Delta T = 4$ s) and time increment $dt = 0.05$ s, in terms of (A) horizontal displacements u_x at point A; (B) vertical displacements u_y at point A. The results are compared with the continuous pulse load solution and to the quadratic HEE solution with the smaller time increment $dt = 0.001$ s

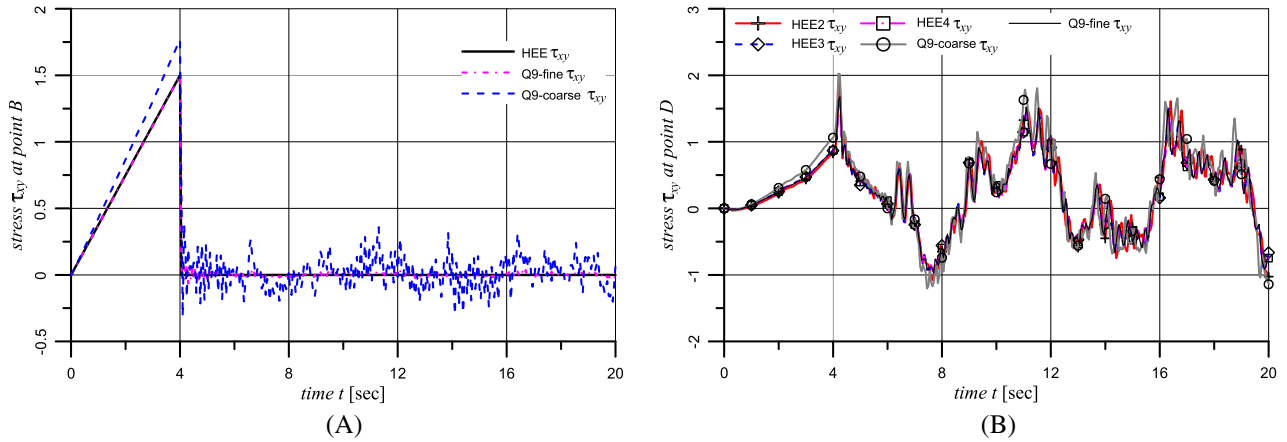

FIGURE 29 Dynamic response of a cantilever beam subjected to a discontinuous pulse tangential load $\boldsymbol{p}_t f_2(t)$ ($\Delta T = 4$ s), in terms of (A) tangential stress τ_{xy} at point B; (B) tangential stress τ_{xy} at point D

point D are plotted in Figure 29B, showing very similar results, and with the equilibrium solutions almost coincident to the converged one, obtained by the DB formulation with fine mesh (Q9 element).

4.2.6 | Slow tangential pulse load for quasi-incompressible material

Finally, the last numerical simulation of a cantilever beam subjected to a dynamic pulse uniform body force $b_y = 0.1$ with a slow loading law ($\Delta T_1 = 8$ s) was performed under a plane strain quasi-incompressible condition with Poisson ratio $\nu = 0.4999$, for which the DB formulation suffers the volumetric locking numerical problem. The numerical results computed with coarse meshes are compared in the graph in Figure 30A in terms of normal stress σ_x at point C, where such component cannot be imposed as a boundary condition, and the results are compared with the converged solution obtained by the fine mesh. The numerical results are plotted in the graph in Figure 30B in terms of tangential stress τ_{xy} and normal stress σ_x at the internal point D, and the results are compared with the converged solution obtained by the fine mesh. The normal stress σ_x at point D in the exact solution is null in the whole time domain, and this result is confirmed by the HEE formulation. The two graphs also show the well-known problems of the DB formulation in evaluation of the normal stress components in quasi-incompressible elastic-dynamic problems.

The numerical results computed with coarse meshes are compared in terms of vertical displacement u_y and horizontal displacement u_x at point A in Figure 31A,B. In the same figure the results are compared with

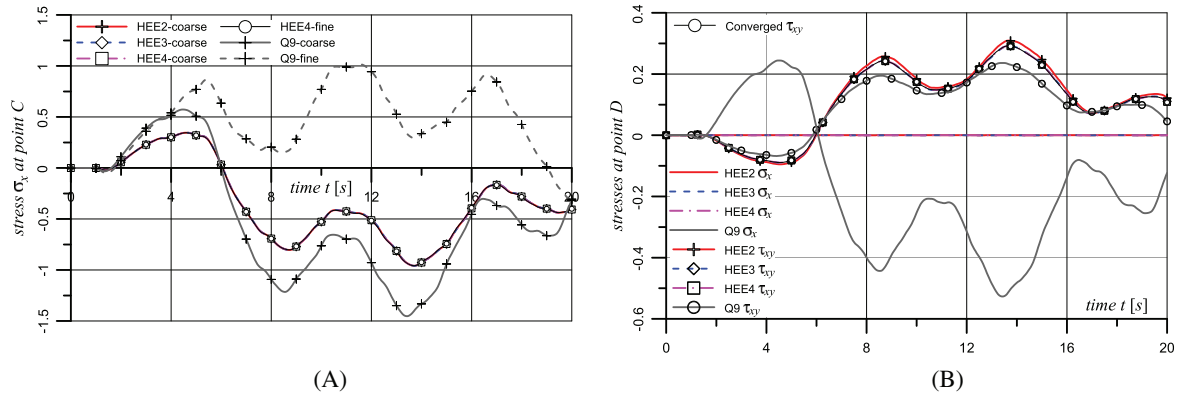

FIGURE 30 Dynamic response of a cantilever beam subjected to the pulse vertical body force load b_y with $\Delta T = 8$ s, in terms of (A) normal stress σ_x at point C; (B) normal stress σ_x and tangential stress τ_{xy} at point D

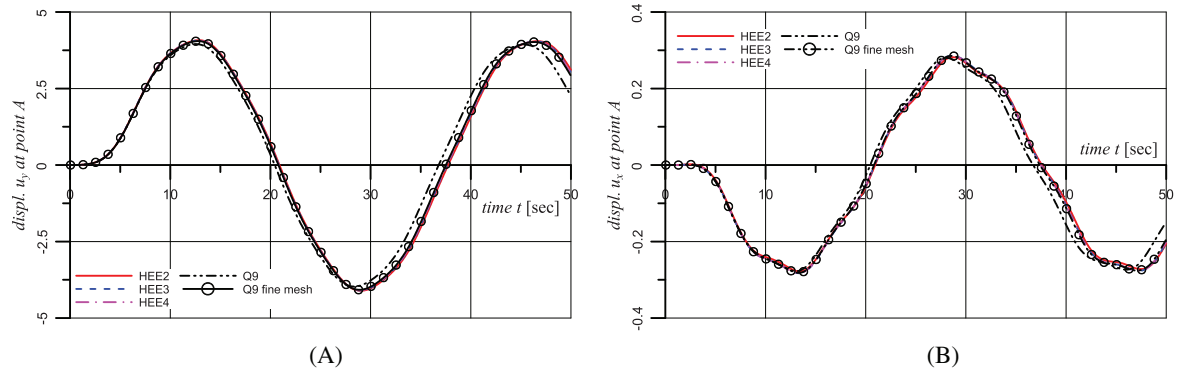

FIGURE 31 Dynamic response of a quasi-incompressible cantilever beam subjected to a uniform vertical body force load b_y with $\Delta T_1 = 8$ s in terms of (A) vertical displacement at point A; (B) horizontal displacement at point A. The results are compared with the Q9 DB numerical solution computed with the fine mesh

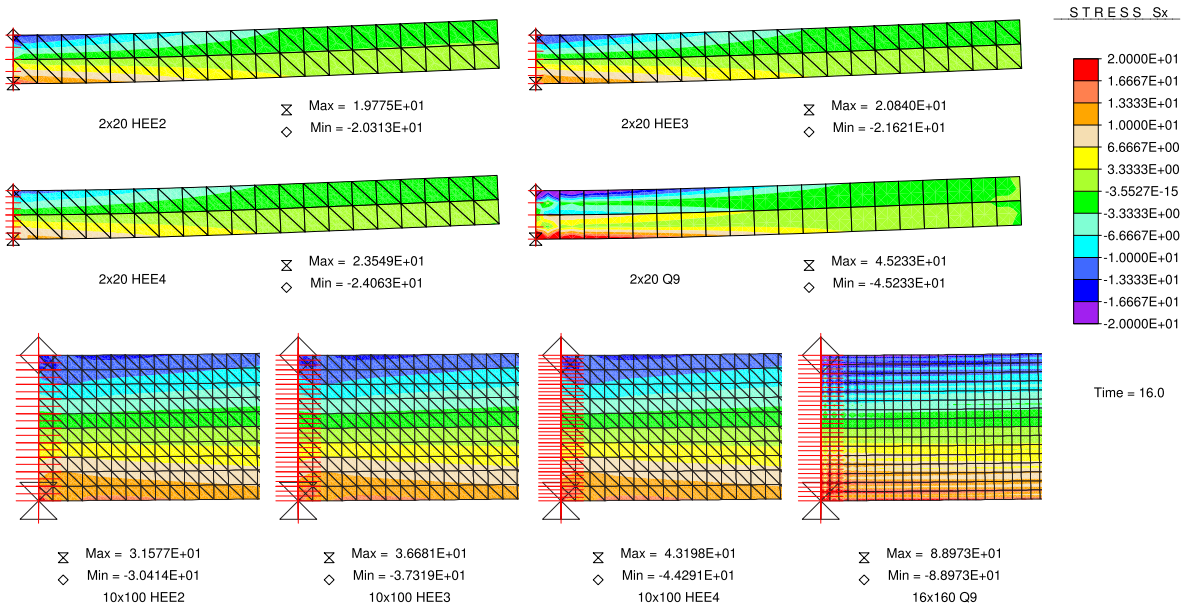

FIGURE 32 Map of normal stress σ_x at time $t = 16$ s for a quasi-incompressible cantilever beam subjected to a pulse vertical body force load b_y with $\Delta T_1 = 8$ s, with coarse mesh and the zoom at the constrained end with fine meshes

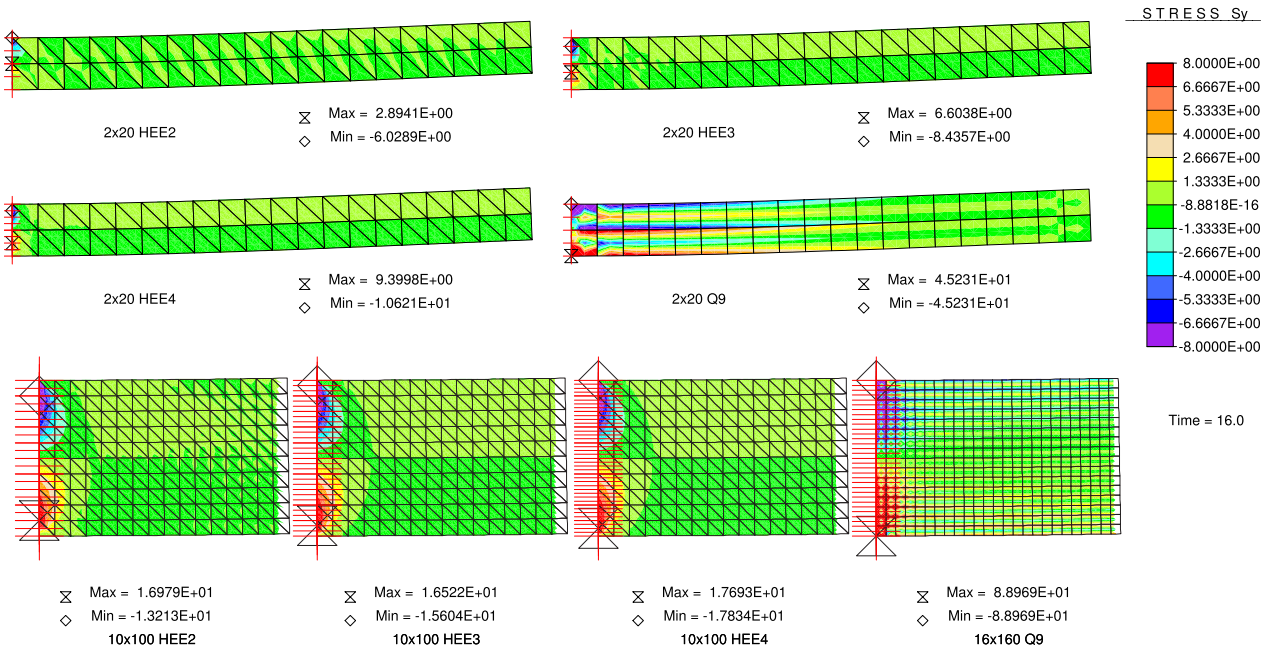

FIGURE 33 Map of normal stress σ_y at time $t = 16$ s for a quasi-incompressible cantilever beam subjected to a pulse vertical body force load b_y with $\Delta T_1 = 8$ s, with coarse mesh and the zoom at the constrained end with fine meshes

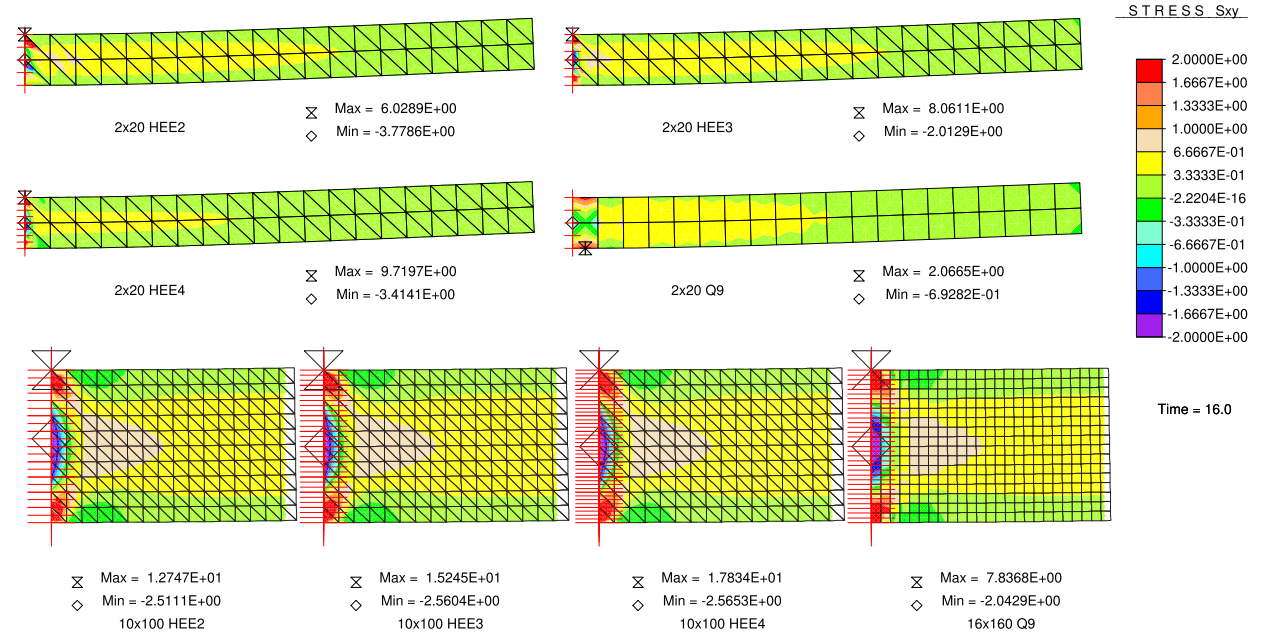

FIGURE 34 Map of tangential stress σ_{xy} at time $t = 16$ s for a quasi-incompressible cantilever beam subjected to a pulse vertical body force load b_y with $\Delta T_1 = 8$ s, with coarse mesh and the zoom at the constrained end with fine meshes

the numerical solution computed with the fine mesh of the Q9 DB formulation, and showing an excellent matching with the three solution obtained with the coarse mesh of the HEE formulation. The better performances of the proposed formulation with respect the classic DB one are clear in the maps of stresses reported in Figures 32–34, where the inconsistent stress distribution of the Q9 DB results are shown for the coarse meshes. The zoom of the constrained end of the fine-mesh solutions are plotted and clearly show the inconsistent stress gradients inside each element. Conversely, the HEE solutions are not affected by any volumetric locking.

5 | CONCLUSIONS

The present article develops the two-dimensional hybrid equilibrium element formulation, with quadratic, cubic, and quartic stress fields, for accurate static and dynamic analyses of both compressible solids and quasi-incompressible ones. The formulation is developed in the variational framework of the minimum complementary energy principle for static analysis and in the variational framework of the Toupin principle, which is the complementary form of the Hamilton principle, for dynamic analysis.

The proposed formulation is defined by independent stress fields for each finite element. The interelement and free boundary equilibrium conditions are applied using a classic hybrid formulation, and an independent displacement field is defined for each element side. The solution provides stress fields which are co-diffusive between adjacent elements and in equilibrium with traction at the free boundary sides. In the static formulation the stress fields verify the domain equilibrium equations. The dynamic formulation is developed under the hypothesis of null initial condition and is based on the impulse field (time integral of stress) and the dynamic equilibrium equation provides the pointwise velocity as the integral of the inertial term. Both the static formulation and the dynamic one are defined with high-order stress field and provide very accurate solutions in terms of stress. The analysis of a Cook membrane static problem and the analysis of a cantilever beam subjected to a pulse dynamic load were performed with several meshes for both compressible and quasi-incompressible elastic material.

The great accuracy of the stress-based proposed formulation is even more evident for static and dynamic analysis of quasi-incompressible materials, for which the classic displacement based formulation comes up against the volumetric locking. Moreover, the static and dynamic HEE formulations represent powerful numerical tools for analysis of elastic solids and also for dual analysis, as well as error estimation of the solutions performed with the classic displacement-based finite element formulations. The drawback of the proposed formulation is the possible presence of spurious kinematic modes, but they are well known and can be controlled or restrained by means of some different approaches.

The main future development of the proposed formulation could be modeling of the interelement fracture and fragmentation phenomena under dynamic load condition, through the approach proposed by the author in Reference 10, where an extrinsic (initially rigid) cohesive interface is embedded at any element side without any remeshing and without additional degrees of freedom. The extrinsic interface can activate once the stress based damaging condition is attained at the element side and the initially rigid behavior of the embedded interfaces does not affect the dynamic response of the pristine material. Conversely, the classic intrinsic interface with initial elastic behavior introduces additional compliance in the overall elastic behavior of a solid with relevant wave propagation issues.

Finally, the extension to nonzero initial conditions represents a basic requirement for analysis of a general elastic-dynamic problem and the static and dynamic analyses of pure incompressible elastic problem represent an interesting topic for further development of the HEE formulation.

ACKNOWLEDGMENTS

The authors wish to thank the anonymous reviewers for their incisive comments and suggestions which are very helpful for improvement of the paper. The financial support of the Italian Ministry for University and Research (MIUR), under the Grant PRIN-2015, Project No. 2015LYYXA8, "Multiscale mechanical models for the design and optimization of microstructured smart materials and metamaterials" is gratefully acknowledged.

CONFLICT OF INTEREST

The authors declare no potential conflict of interests.

DATA AVAILABILITY STATEMENT

The datasets generated and analyzed during the current study are available from the corresponding author on reasonable request.

ORCID

Francesco Parrinello https://orcid.org/0000-0002-9511-7177

REFERENCES

1. Fraeijs de Veubeke B. *Upper and Lower Bounds in Matrix Structural Analysis*. Vol 72. Liège, Belgium: LTAS; 1963:165-201.

2. Fraeijs de Veubeke B. Chapter 9. Displacement and equilibrium models in the finite element method. In: Zienkiewicz OC, Holister GS, eds. *Stress Analysis*. London, UK: Wiley; 1965.
3. de Almeida JPM, de Freitas JAT. An alternative approach to the formulation of hybrid equilibrium finite elements. *Comput Struct*. 1991;40:1043-1047.
4. Pereira OJBA. Hybrid equilibrium hexahedral elements and super-elements. *Commun Numer Methods Eng*. 2008;24:157-165.
5. de Almeida JPM, Pereira OJBA. A set of hybrid equilibrium finite element models for the analysis of three-dimensional solids. *Int J Numer Methods Eng*. 1996;39(16):2789-2802.
6. Kempeneers M, Debongnie JF, Beckers P. Pure equilibrium tetrahedral finite elements for global error estimation by dual analysis. *Int J Numer Methods Eng*. 2010;81:513-536.
7. Pereira OJBA, de Almeida JPM, Maunder EA. Adaptive methods for hybrid equilibrium finite element models. *Comput Methods Appl Mech Eng*. 1999;176:19-39.
8. de Almeida JPM, Reis J. An efficient methodology for stress-based finite element approximations in two-dimensional elasticity. *Int J Numer Methods Eng*. 2020;121(20):4649-4673. https://doi.org/10.1002/nme.6458
9. Zienkiewicz OC, Taylor RL, Zhu JZ. Chapter 10. Incompressible problems, mixed methods, and other procedures of solution. In: Zienkiewicz O, Taylor R, Zhu J, eds. *The Finite Element Method: Its Basis and Fundamentals*. 7th ed. Oxford, UK: Butterworth-Heinemann; 2013:315-359.
10. Parrinello F. Hybrid equilibrium element with interelement interface for the analysis of delamination and crack propagation problems. *Int J Numer Methods Eng*. 2020. https://doi.org/10.1002/nme.6531
11. Parrinello F, Failla B, Borino G. Cohesive-frictional interface constitutive model. *Int J Solids Struct*. 2009;46(13):2680-2692.
12. Parrinello F, Marannano G, Borino G. A thermodynamically consistent cohesive-frictional interface model for mixed mode delamination. *Eng Fract Mech*. 2016;153:61-79. https://doi.org/10.1016/j.engfracmech.2015.12.001
13. Parrinello F, Borino G. Non associative damage interface model for mixed mode delamination and frictional contact. *Eur J Mech A Solids*. 2019;76:108-122.
14. Noels L, Radovitzky R. An explicit discontinuous Galerkin method for non-linear solid dynamics: formulation, parallel implementation and scalability properties. *Int J Numer Methods Eng*. 2008;74(9):1393-1420. https://doi.org/10.1002/nme.2213
15. Radovitzky R, Seagraves A, Tupek M, Noels L. A scalable 3D fracture and fragmentation algorithm based on a hybrid, discontinuous Galerkin, cohesive element method. *Comput Methods Appl Mech Eng*. 2011;200(1-4):326-344. https://doi.org/10.1016/j.cma.2010.08.014
16. Olesen K, Gervang B, Reddy JN, Gerritsma M. A higher-order equilibrium finite element method. *Int J Numer Methods Eng*. 2018;114(12):1262-1290. https://doi.org/10.1002/nme.5785
17. Zhang Y, Fisser J, Gerritsma M. A hybrid mimetic spectral element method for three-dimensional linear elasticity problems. *J Comput Phys*. 2021;433:110179. https://doi.org/10.1016/j.jcp.2021.110179
18. Parrinello F. Restraining approach for the spurious kinematic modes in hybrid equilibrium element. *Comput Mech*. 2013;52(4):885-901. https://doi.org/10.1007/s00466-013-0851-x
19. Maunder EAW, de Almeida JPM, Ramsay ACA. A general formulation of equilibrium macro-elements with control of spurious kinematic modes: the exorcism of an old curse. *Int J Numer Methods Eng*. 1996;39:3175-3194.
20. Maunder EAW, de Almeida JPM. Hybrid-equilibrium elements with control of spurious kinematic modes. *Compute Assist Mech Eng Sci*. 1997;4:587-605.
21. Wang L, Zhong H. A traction-based equilibrium finite element free from spurious kinematic modes for linear elasticity problems. *Int J Numer Methods Eng*. 2014;99(10):763-788. https://doi.org/10.1002/nme.4701
22. Fraeijs de Veubeke B. *The Dual Principles of Elastodynamics: Finite Element Applications. Technical Report*. Liége, Belgium: Université de Liége; 1971.
23. Geradin M. Special applications of Hamiltons's principle to structural dynamics. In: Glowinski R, Lions JL, Laboria I, eds. *Computing Methods in Applied Sciences and Engineering, 1977*. Vol I. Berlin/Heidelberg, Germany: Springer; 1979:222-238.
24. de Freitas JAT. Formulation of elastostatic hybrid-Trefftz stress elements. *Comput Methods Appl Mech Eng*. 1998;153(1):127-151. https://doi.org/10.1016/S0045-7825(97)00042-X
25. de Freitas JAT. Hybrid finite element formulations for elastodynamic analysis in the frequency domain. *Int J Solids Struct*. 1999;36(13):1883-1923. https://doi.org/10.1016/S0020-7683(98)00064-X
26. de Freitas JAT, Wang Z. Elastodynamic analysis with hybrid stress finite elements. *Comput Struct*. 2001;79(19):1753-1767. https://doi.org/10.1016/S0045-7949(01)00106-7
27. Wang L, Lu ZR, Liu ZQ. Complementary energy principle for elastodynamics: Free of volumetric locking. *Int J Solids Struct*. 2017;120:103-114. https://doi.org/10.1016/j.ijsolstr.2017.04.032
28. Nguyen CU, Ibrahimbegovic A. Hybrid-stress triangular finite element with enhanced performance for statics and dynamics. *Comput Methods Appl Mech Eng*. 2020;372:113381. https://doi.org/10.1016/j.cma.2020.113381
29. Nguyen CU, Ibrahimbegovic A. Visco-plasticity stress-based solid dynamics formulation and time-stepping algorithms for stiff case. *Int J Solids Struct*. 2020;196-197:154-170. https://doi.org/10.1016/j.ijsolstr.2020.04.018
30. Ervin VJ. Computational bases for RTk and BDMk on triangles. *Comput Math Appl*. 2012;64(8):2765-2774. https://doi.org/10.1016/j.camwa.2012.08.011
31. de Almeida JPM, Maunder EAW. *Equilibrium Finite Element Formulations*. Hoboken, NJ: John Wiley & Sons, Ltd; 2016.
32. de Almeida JPM, Maunder EAW. Improved eigenfrequencies of mechanical systems by combining complementary models. *Int J Numer Methods Eng*. 2018;114(12):1310-1330. https://doi.org/10.1002/nme.5787

33. Toupin RA. A variational principle for the mesh-type analysis of a mechanical system. *J Appl Mech Trans ASME*. 1952;19(2):151-152.
34. Tabarrok B. Complementary variational principles in elastodynamics. *Comput Struct*. 1984;19(1):239-246 Special Memorial Issue. https://doi.org/10.1016/0045-7949(84)90223-2
35. Maunder EAW, de Almeida JPM. The stability of stars of triangular equilibrium plate elements. *Int J Numer Methods Eng*. 2009;77:922-968.
36. Harrison HR, Nettleton T. Hamilton's principle. In: Harrison H, Nettleton T, eds. *Advanced Engineering Dynamics*. Vol 3. London, UK: Butterworth-Heinemann; 1997:46-54.
37. Zienkiewicz OC, Taylor RL. *The Finite Element Method*. 5th ed. Oxford, UK: Butterworth-Heinemann Press; 2000.
38. Cook RD. Improved two-dimensional finite element. *J Struct Div*. 1974;100(ST6):1851-1863.
39. Liu GR, Nguyen-Thoi T, Lam KY. A novel alpha finite element method (αFEM) for exact solution to mechanics problems using triangular and tetrahedral elements. *Comput Methods Appl Mech Eng*. 2008;197(45):3883-3897. https://doi.org/10.1016/j.cma.2008.03.011
40. de Almeida JPM, Maunder EAW. Recovering local equilibrium from three-dimensional compatible finite element solutions. *Int J Numer Methods Eng*. 2020;121(12):2783-2805. https://doi.org/10.1002/nme.6332
41. de Almeida JPM, Pereira OJBA. Upper bounds of the error in local quantities using equilibrated and compatible finite element solutions for linear elastic problems. *Comput Methods Appl Mech Eng*. 2006;195:279-296.
42. Wang L, Zhong H. A unified approach to strict upper and lower bounds of quantities in linear elasticity based on constitutive relation error estimation. *Comput Methods Appl Mech Eng*. 2015;286:332-353. https://doi.org/10.1016/j.cma.2014.12.003

How to cite this article: Parrinello F, Borino G. Hybrid equilibrium element with high-order stress fields for accurate elastic dynamic analysis. *Int J Numer Methods Eng*. 2021;1–33. https://doi.org/10.1002/nme.6793

APPENDIX A. HIGH-ORDER STATIC COEFFICIENT MATRICES

The two-dimensional stress components are defined as functions of the Cartesian coordinates in Equations (2)–(4) for the quadratic formulation and are represented in Equation (5) in the Voigt notation. The coefficient matrix $\mathbf{S}_e(\mathbf{x})$ and the vector $\mathbf{a}_e$ of the generalized stress variables are defined as follows:

$$\mathbf{S}_e(\mathbf{x}) = \begin{bmatrix} 1 & y & y^2 & 0 & 0 & 0 & 0 & 0 & -x & -x^2/2 & 0 & -2xy \\ 0 & 0 & 0 & 1 & x & x^2 & 0 & -y & 0 & -y^2/2 & -2xy & 0 \\ 0 & 0 & 0 & 0 & 0 & 0 & 1 & x & y & xy & x^2 & y^2 \end{bmatrix}, \tag{A1}$$

$$\mathbf{a}_e = \begin{bmatrix} a_1 & a_2 & a_3 & a_4 & a_5 & a_6 & a_7 & a_8 & a_9 & a_{10} & a_{11} & a_{12} \end{bmatrix}^T, \tag{A2}$$

for the quadratic formulation ($n_s = 2$, $n_a = 12$),

$$\mathbf{S}_e(\mathbf{x}) = \begin{bmatrix} 1 & y & y^2 & y^3 & 0 & 0 & 0 & 0 & 0 & 0 & -x & -x^2/2 & 0 & -2xy & -x^3/3 & -x^2y & 0 & -3xy^2 \\ 0 & 0 & 0 & 0 & 1 & x & x^2 & x^3 & 0 & -y & 0 & -y^2/2 & -2xy & 0 & -xy^2 & -y^3/3 & -3x^2y & 0 \\ 0 & 0 & 0 & 0 & 0 & 0 & 0 & 0 & 1 & x & y & xy & x^2 & y^2 & x^2y & xy^2 & x^3 & y^3 \end{bmatrix}, \tag{A3}$$

$$\mathbf{a}_e = \begin{bmatrix} a_1 & a_2 & a_3 & \dots & a_{16} & a_{17} & a_{18}, \end{bmatrix}^T \tag{A4}$$

for the cubic formulation ($n_s = 3$, $n_a = 18$), and

$$\mathbf{S}_e(\mathbf{x}) = \begin{bmatrix} 1 & y & y^2 & y^3 & y^4 & 0 & 0 & 0 & 0 & 0 & 0 & 0 & -x & -x^2/2 & 0 & -2xy & -x^3/3 \\ 0 & 0 & 0 & 0 & 0 & 1 & x & x^2 & x^3 & x^4 & 0 & -y & 0 & -y^2/2 & -2xy & 0 & -xy^2 \\ 0 & 0 & 0 & 0 & 0 & 0 & 0 & 0 & 0 & 0 & 1 & x & y & xy & x^2 & y^2 & x^2y \end{bmatrix}$$
$$\begin{bmatrix} -x^2y & 0 & -3xy^2 & -x^4/4 & -2/3x^3y & -3/2x^2y^2 & 0 & -4y^3x \\ -y^3/3 & -3x^2y & 0 & -3/2x^2y^2 & -2/3y^3x & -y^4/4 & -4x^3y & 0 \\ xy^2 & x^3 & y^3 & x^3y & x^2y^2 & xy^3 & x^4 & y^4 \end{bmatrix}, \tag{A5}$$

$$\mathbf{a}_e = \begin{bmatrix} a_1 & a_2 & a_3 & \dots & a_{23} & a_{24} & a_{25}, \end{bmatrix}^T \tag{A6}$$

for the quartic formulation ($n_s = 4$, $n_a = 25$).

APPENDIX B. HIGH-ORDER DYNAMIC COEFFICIENT MATRICES

The two-dimensional impulse components of the elastic-dynamic problem are defined as functions of the Cartesian coordinates in Equation (30) for the quadratic formulation in the Voigt notation. For the quadratic formulation ($n_s = 2$, $n_a = 18$), the coefficient matrices $\mathbf{S}_e^{(2)}(\mathbf{x})$ is defined in Equation (30), the matrix of divergence of impulse $\mathbf{T}_e^{(2)}(\mathbf{x})$ is defined in Equation (33) and the vector of generalized variable is $\mathbf{a}_e^{(2)} = [a_1 a_2 a_3 \dots a_{16} a_{17} a_{18}]$. For the cubic formulation ($n_s = 3$, $n_a = 30$) the vector of generalized variable and the coefficient matrices can be written in the following compact notation: $\mathbf{a}_e^{(3)} = \left[\mathbf{a}_e^{(2)} \mathbf{a}_e^{(2-3)}\right]$, $\mathbf{S}_e^{(3)} = \left[\mathbf{S}_e^{(2)} \mathbf{S}_e^{(2-3)}\right]$ and $\mathbf{T}_e^{(3)} = \left[\mathbf{T}_e^{(2)} \mathbf{T}_e^{(2-3)}\right]$ with

$$\mathbf{a}_e^{(2-3)} = \begin{bmatrix} a_{13} & \dots & a_{28} & a_{29} & a_{30} \end{bmatrix}^T, \tag{B1}$$

$$\mathbf{S}_e^{(2-3)} = \begin{bmatrix} x^3 & 0 & 0 & x^2y & 0 & 0 & x.y^2 & 0 & 0 & y^3 & 0 & 0 \\ 0 & x^3 & 0 & 0 & x^2y & 0 & 0 & x.y^2 & 0 & 0 & y^3 & 0 \\ 0 & 0 & x^3 & 0 & 0 & x^2y & 0 & 0 & xy^2 & 0 & 0 & y^3 \end{bmatrix}, \tag{B2}$$

$$\mathbf{T}_e^{(2-3)} = \begin{bmatrix} 3x^2 & 0 & 0 & 2xy & 0 & x^2 & y^2 & 0 & 2xy & 0 & 0 & 3y^2 \\ 0 & 0 & 3x^2 & 0 & x^2 & 2xy & 0 & 2xy & y^2 & 0 & 3y^2 & 0 \end{bmatrix}. \tag{B3}$$

For the quartic formulation ($n_s = 4$, $n_a = 45$) the vector of generalized variable and the coefficient matrices can be written in the following compact notation: $\mathbf{a}_e^{(4)} = \left[\mathbf{a}_e^{(3)} \mathbf{a}_e^{(3-4)}\right]$, $\mathbf{S}_e^{(4)} = \left[\mathbf{S}_e^{(3)} \mathbf{S}_e^{(3-4)}\right]$, and $\mathbf{T}_e^{(4)} = \left[\mathbf{T}_e^{(3)} \mathbf{T}_e^{(3-4)}\right]$ with

$$\mathbf{a}_e^{(3-4)} = \begin{bmatrix} a_{31} & \dots & a_{43} & a_{44} & a_{45} \end{bmatrix}^T, \tag{B4}$$

$$\mathbf{S}_e^{(3-4)} = \begin{bmatrix} x^4 & 0 & 0 & x^3y & 0 & 0 & x^2y^2 & 0 & 0 & xy^3 & 0 & 0 & y^4 & 0 & 0 \\ 0 & x^4 & 0 & 0 & x^3y & 0 & 0 & x^2y^2 & 0 & 0 & xy^3 & 0 & 0 & y^4 & 0 \\ 0 & 0 & x^4 & 0 & 0 & x^3y & 0 & 0 & x^2y^2 & 0 & 0 & xy^3 & 0 & 0 & y^4 \end{bmatrix}, \tag{B5}$$

$$\mathbf{T}_e^{(3-4)} = \begin{bmatrix} 4x^3 & 0 & 0 & 3x^2y & 0 & x3 & 2xy^2 & 0 & 2yx^2 & y^3 & 0 & 3xy^2 & 0 & 0 & 4y^3 \\ 0 & 0 & 4x^3 & 0 & x^3 & 3x2y & 0 & 2x^2y & 2y^2x & 0 & 3y^2x & y^3 & 0 & 4y^3 & 0 \end{bmatrix}. \tag{B6}$$